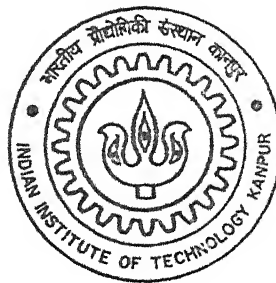# AN EXPERIMENTAL STUDY OF AERODYNAMIC CHARACTERISTICS OF A TWO-ELEMENT AIRFOIL

by

K.S. Venkateswara Reddy

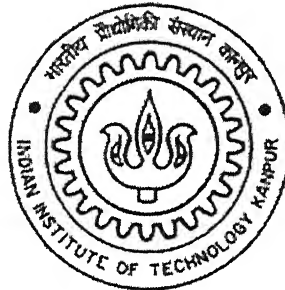**DEPARTMENT OF AEROSPACE ENGINEERING**

Indian Institute of Technology Kanpur

DECEMBER, 2002

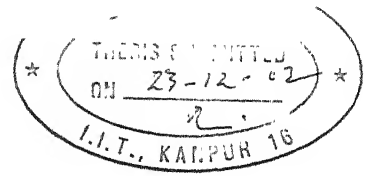# AN EXPERIMENTAL STUDY OF AERODYNAMIC CHARACTERISTICS OF A TWO-ELEMENT AIRFOIL

A *Thesis* Submitted
in partial Fulfillment of the Requirement for the
Degree of Master of Technology

By
K.S.VENKATESWARA REDDY

To
DEPARTMENT OF AEROSPACE ENGINEERING
INDIAN INSTITUTE OF TECHNOGY, KANPUR
December 2002

CERTIFICATE

It is certified that the work contained in this thesis entitled *"AN EXPERIMENTAL STUDY OF AERODYNAMIC CHARACTERISTICS OF A TWO-ELEMENT AIRFOIL"*, by K.S.Venkateswara Reddy, has been carried out under my supervision and that this work has not been submitted elsewhere for any degree.

Dr. Kamal Poddar

Department of Aerospace Engineering
Indian Institute of Technology, Kanpur.

ACKNOWLEDGEMENT

Dedicated
to
My Loving Parents

TABLE OF CONTENTS

LIST OF TABLES

LIST OF FIGURES

NOMENCLATURE

C	Chord length (retracted position)
C_A	Coefficient of force along chord
C_{Af}	Coefficient of force along chord of flap
C_{Am}	Coefficient of force along chord of main element
C_d	Coefficient of drag
C_l	Coefficient of lift
C_{mle}	Pitching moment coefficient about leading edge
C_{mlef}	Pitching moment coefficient about the leading edge of main element due to flap
C_{mlem}	Pitching moment coefficient about the leading edge of main element due to main element
C_N	Coefficient of normal force perpendicular the chord
C_{Nf}	Coefficient of normal force perpendicular the chord of flap
C_{Nm}	Coefficient of normal force perpendicular the chord of main element
C_p	Coefficient of pressure
G	Gap
OH	Over hang
P_l	Pressure on the lower surface
P_u	Pressure on the upper surface
P_∞	Free stream pressure
Q_∞, Q_{inf}	Free stream dynamic head

S	Wing area
TTS	Turntable speed
U	Velocity in the wake
U_∞, U_{inf}	Free stream velocity
X	Distance along the chord from the leading edge
Y	Wake port distance from the tunnel centerline
α	Angle of attack
δ_f	Flap deflection
ρ	Density of air

ABSTRACT

An experimental investigation on the two-element airfoil was carried out at the National Wind Tunnel Facility, IIT Kanpur to study the hysteresis effect and the effect of flap deflection and overhang on the aerodynamic characteristics. Experiments were conducted for retracted configuration and flap deflected configurations with 5.23%, 0% and -1.3% overhang. Flap deflected tests were conducted at fixed gap of 2.61% and at chord Reynolds number 1.53×10^6. Six pressure scanners were used for airfoil surface pressure and wake pressure measurements. During the tests angle of attack of the airfoil was varied from -10^0 to 30^0 in discrete steps. From the pressure measurements lift, drag and pitching moment about the leading edge were calculated.

Flap retracted configuration showed significant hysteresis in the sectional properties as well in the surface pressure distribution during pitch-up and pitch-down mode near the stall. Results of flap deflected configurations also showed similar hysteresis effect in the sectional properties. The hysteresis loop was significantly increased due to flap deflection in the present investigation. Flap deflection was found to increase lift, drag, and pitching moment about the leading edge and decrease the stall angle as compared with the retracted configuration. The stall was more severe for the flap deflected configurations. Results of zero overhang showed increase in lift as compared with both positive and negative overhangs. But in drag and pitching moment coefficients, increasing trend is observed for negative overhang as compared with positive and zero overhangs. It appears from the surface pressure distribution that the movement of separation point towards leading edge during pitch-up mode is slower than the movement towards trailing edge during pitch-down mode. This is responsible for hysteresis in the sectional properties near the stall angles.

1 - INTRODUCTION

1.1 Introduction

Transport aircraft wings must be designed to operate in the entire envelope including cruise and low speed conditions. Earlier airplanes did not require high-lift systems because of their low wing loadings and low speed ratios between cruise and low speed conditions. In contrast, modern commercial transport aircraft have higher cruise speeds and wing loadings; consequently, a high-lift system is required to provide additional lift necessary for low speed operations. High-lift system plays an important role to improve the airport capacity, through a reduction of airplane's wake vortices, allowing more frequent take-off and landing of subsequent flights. As a result current and future aircraft design trends are in favor of developing high lift producing systems.

As conventional single element airfoils are unable to develop high lift to meet modern aircraft requirements, current research is focused on multi-element airfoils. The multi-element airfoils generally have two or more elements, e.g. a main element with a trailing edge flap or a main element with leading edge slat and trailing edge single segment flap or double segment flap. Although, increasing the number of elements increases the lift at the same time flow complexity, mechanical complexity and economic burden increases.

High-lift systems have traditionally been mechanically complex and they generally consist of some combinations of leading edge slats and single or multiple trailing edge flaps. The current design trends in high-lift system for modern transport aircraft is towards mechanically simpler single segment flap that maintains high levels of maximum lift while minimizing flow separation. Furthermore, reducing the number of elements in high lift systems and maintaining attached flow on the flap also reduces aircraft noise.

Modern aircraft wings are aerodynamically designed to operate for a range of flying conditions within their performance limitations. Their flaps are retracted during

cruise conditions (having low lift and drag for fuel economy) and deflected during takeoff for high lift generation (to reduce take-off distance), high C_{Lmax} and drag during landing (to reduce speed), and high lift to drag ratio during climbing (to reduce engine thrust). Thus, multi-element airfoil with trailing edge flaps plays a crucial role in aircraft performance. Within the spectrum of operation, there should be a harmony between the interacting elements, say for two element airfoils between the main element and flap. This harmony provides the type of flow field that is not in conflict with its boundaries, but has the same design point for both increasing and decreasing angles of attack. For actual flight conditions any irreversibility in the airfoil performance needs to be known prior to use. Considering the scale effects, this can be determined by wind tunnel testing.

1.2 Literature survey

Fundamental to the operation of all airplanes is the production of lift by their wings, and as a result, the need to know exactly how much lift a certain wing will produce while operating under various conditions is a priority in the field of aerodynamics. Generally, wind tunnel testing is carried out to understand and evaluate the performance of wings and airfoils.

Flaps are wing trailing edge devices used to reduce the takeoff and landing distances of aircraft by increasing the maximum lift coefficient of the wing. Due to deployment of flap, lift produced by a multi-element airfoil is more than the single element airfoil at the same angle of attack, for two reasons. Firstly, the effective camber of the airfoil is increased; secondly, the wing area is increased by the overhang of flap (as shown in figure 3). Flow over a two element airfoil differs from the single element airfoil as the pressure distribution is affected by the interaction of the wake of the main element and boundary layer on the flap's suction surface. According to Meredith (1993) some of the viscous features that affect multi-element airfoils include boundary layer transition, viscous wake interactions and confluent wakes flows. Some important insights into the physical process that govern the flow in the gaps of multi-element airfoil over single element airfoil were summarized by Smith (1975). In his extensive survey of high-lift systems, he reviewed development

of high-lift airfoils and lift limits in potential flows. He also described the primary effects of gap and the circulation of the downstream elements. According to him, (the downstream element induces) near the trailing edge region of the upstream element, high velocity which is inclined to the mean line at the rear of the forward element. Such flow inclination induces considerable circulation on the forward element. Also, the trailing edge of the forward element is in a region of velocity appreciably higher than free-stream. The higher discharge velocity on the leeside of the flap relieves the pressure rise impressed on the boundary layer thus alleviating separation problems permitting increased lift. As the boundary layer from forward elements is dumped at velocities appreciably higher than free-stream, the final deceleration to free-stream velocity is done in an efficient manner. Each new element starts out with a fresh boundary layer at its leading edge. Thin boundary layers withstand stronger adverse pressure gradients than thicker ones.

As the angle of attack of an airfoil increases beyond a certain value, the airfoil stalls and the massive flow separation on the airfoil surface results in sharp drop in lift and increase in the drag. In certain cases, the stall is accompanied by hysteresis in the flow. When angle of attack is increased beyond the stall and then decreased, there is a difference in aerodynamic performance during this increasing and decreasing angle of attack. This is called hysteresis in the flow. The hysteresis associated stall is discussed below as studied by many researchers.

Hoffman (1991) has reported results for an experimental study for flow past NACA 0015 airfoil at $Re = 250000$. He observed hysteresis loop in the aerodynamic coefficients. Hysteresis has also been reported by Biber and Zumwalt (1993) on a two-element GA(W)-2 airfoil and it was found to be function of the angle of flap deployment, gap geometry and the history of changes in air speed or angle of attack. They also found that the hysteresis is not restricted to low Reynolds number flows but can also be found at relatively high Reynolds number. The Reynolds number for their experiments was 2.2×10^6. Marchman (1985) also observed hysteresis near the stall for an aspect ratio 8, Wortmann FX-63-137, untapered, unswept wing at chord-based Reynolds numbers of 70,000-300,000.

Mittal and Saxena (2002) observed hysteresis in the aerodynamic coefficients, from their computational study, for flow past NACA0012 airfoil at a Reynolds number of 10^6 for a small range of angle of attack close to the stall. They reasoned that the hysteresis is due to the difference in the location of the separation point of the flow on the upper surface of the airfoil during the increasing and decreasing angles of attack.

Biber and Zumwalt (1993) conducted experiments on GA(W)-2 airfoil with 25% slotted flap at a Reynolds number 2.2 $\times 10^6$ and Mach number 0.13 for flap deflections of 30^0 and 40^0 with optimum gap and narrow gap. They observed an abrupt loss of lift after reaching maximum lift for certain flap deflection angle. This was followed by a nearly constant lift and then again sudden loss of lift as the angle of attack was increased. The higher the flap angle, the larger is the drop in lift and wider is the flat line. They interpreted these features as a two-stage stall in which stall on the flap followed by the stall on the main element.

Details of two-stage stall are explained in another paper by Biber (1993) and the same is summarized here. As a result of flap deployment the flow around the flap is very complex due to the interactions between different layers of flow. The boundary layer flow over the main wing is thick and turbulent for the most of the wing. It separates at wing trailing edge and extends over the flap as a wake with adverse pressure gradient at low angles of attack. On the other hand boundary layer over the flap is thin and laminar and tends to remain so due to favorable pressure gradient. This favorable pressure gradient is provided by the slot flow passing through the gap. This flow is highly accelerated potential flow with low pressure compared to neighboring flows. This low-pressure region creates strong pressure gradients across the flow just above the flap. Near stall angles, the separating streamline at the wing trailing edge can't resist the adverse pressure gradients and starts moving just upstream of the trailing edge. When this happens, the boundary layer becomes free of strong wake influence. Now boundary layer becomes thicker and stronger, with slight increase of angle of attack the flow separates on the flap, after that the separating streamline moves further upstream on the main element. Like this two-stage stall, first on the flap then on the wing occurs.

Adair and Horne (1989) have conducted experiments on a two-element airfoil with flap deflection 21.8^0, gap 3.5%, and overhang 2.8% at an angle of attack 8.2^0 to understand the flow in the vicinity of the flap. The flow around the flap was observed to be complex due to the presence of strong initially inviscid jet emanating from the slot between airfoil and flap, and gradually merging of the main element wake and flap suction side boundary layer. The flow in the vicinity of the main airfoil trailing edge was subjected to adverse pressure gradients with no boundary layer separation present, but in the vicinity of the flap trailing edge, where a small region of boundary layer separation extended over the aft 7% of flap chord. Rogers (1993) simulated flow over the same two-element airfoil used by the Adair and Horne (1989) by using a turbulence model. He found some discrepancy with the experimental data and reasoned that this is most likely due to wind tunnel wall effects.

Nakayama (1990) has presented experimental investigation of flow field over a multi-element airfoil for two test conditions; one is close to takeoff configuration with 15^0 flap deflection and 10^0 angle of attack having attached boundary layers and moderately thick wake, and the other configuration is for higher lift case with 30^0 flap deflection and 18^0 angle of attack. He observed that many parts of shear flow deviated vastly from classical flows and the interaction with external flow is very strong.

An important practical problem in wind tunnel testing of multi-element airfoils is the requirement to test a range of configurations to ensure that the optimum configuration is chosen. Unfortunately, this is very time consuming if one considers all the variables such as flap position (gap, overhang) and deflection, angle of attack and also Reynolds and Mach number effects. Lin and Dominick (1997) conducted experiments on a three-element airfoil to study the effects of variation of gaps and overhangs of slat and flap. They observed separations for negative overhang cases, this is especially important since a separated flow generates increased drag and associated noise and vibrations, and possibly less lift than attached flow.

Volarzo and Dominick (1991) have conducted experiments to optimize maximum lift at high Reynolds number. They achieved maximum lift coefficient of 4.5 with three element airfoil (leading edge slat and trailing edge flap) and 5.0 with

double segment flaps. They also observed the differences in optimum riggings between single segment and double segment flaps, Reynolds number effects on maximum lift coefficient. In another paper (1993) they studied Reynolds and Mach number effects on takeoff and landing configurations. They observed Mach number effects are more pronounced at lower Reynolds number; while, Reynolds number effects are minimal on both lift and drag for takeoff configuration. However, significant Reynolds number effects are observed on the maximum lift for landing configuration.

1.3 Objective of present study

The objectives of present investigation are

1. To study the effect of trailing edge flap deflections and overhang positions on the aerodynamic performance of a two-element airfoil,

2. To study the effect of angle of attack for each setting of retracted and flap configuration, and

3. To study the behavior of aerodynamic characteristics and hysteresis effect near the stall.

2 - EXPERIMENTAL ARRANGEMENT

Experiments were conducted at the National Wind Tunnel Facility (NWTF), IIT Kanpur. Two-element airfoil model was mounted vertically inside the test section on a turntable and the rotation of the turntable provided various angles of attack. Electronic Pressure scanners were used to measure the surface pressure on the model and wake profile in the airfoil wake by using a rake. Airfoil sectional properties were calculated from the surface pressure distribution and wake profile. Control of turntable rotation and data acquisition were done using sophisticated instrumentation based on Virtual Instrumentation (VI) concept.

2.1 Experimental Facility

National Wind Tunnel Facility (NWTF) is a low speed closed circuit wind tunnel with associated equipment and modern instrumentation. It has interchangeable test sections having cross section 3 m × 2.25 m. The test section is split into two parts an upstream and a downstream part. This facilitates four combinations of two upstream and two downstream parts. Length of upstream part of the test section is 5.75 m and downstream part is 3 m. The aerodynamic layout of tunnel circuit is shown in figure 1, which elaborates its design features. Wide-angle diffuser with contraction ratio 9:1 is provided before the settling chamber. Maximum wind speed is 80 m/s with Reynolds number 6×10^6 /m and it has four anti-turbulence screens, free stream turbulence is less than 0.1% and maximum flow angularity is 0.2^0. Wind is blown by a fan and drive system. The fan consists of a 12-bladed rotor followed by a 7-bladed stator and is driven by the 1000kw power, constant rated DC motor.

2.2 Model fabrication

Model for the present investigation was a two-element airfoil having a chord length of 0.765 m for retracted configuration and a span of 1 m. The length of the main element was 0.665m and the flap chord length was 0.24 m. This ensured tunnel blockage to less than 10% for angles of attack up to 30°.

The airfoil model was fabricated out of solid teak wood blocks with Perspex airfoil section at mid-span for installing chordwise pressure taps both on the upper and lower surfaces of the main element and flap. Two square spurs through the airfoil spanning the tunnel height were used as main load bearing member. To ensure the accuracy of the aerofoil fabrication, templates were made at 1:1 scale using data from Bonnhaus and Anderson (1995) as given in tables 1a and 1b.

2.3 Experimental Setup

The two-element airfoil model was mounted on the bottom turntable and was also fixed to the upper turntable in such a manner that the mid chord of the aerofoil coincided with the centre of the turntable. The model was aligned to set the angle formed between the tunnel centre line and the model chord line to zero degree (within $\pm 0.02^0$ accuracy). Turntables at NWTF are powered by feedback controlled angle setting system. Both the turntables (floor and roof) are driven in synchronous mode. Airfoil model in retracted configuration is shown in figure 2a with endplate and mounting bars in figure 2b.

Geometric location of the flap relative to main element is specified by the gap, overhang and deflection. The definition of gap, overhang and flap deflection is shown in figure 3.

2.4 Pressure port details

Surface pressure measurements were made with 85 pressure ports on the model. These pressure ports were located chordwise at mid span both on upper and lower surfaces of main element and flap. Pressure ports were mounted on the surface of the airfoil by inserting steel tubes which were inserted to the aerofoil surface and projecting inside the model. These tubes were then connected by PVC tubes to the electronically scanned pressure (ESP) measurement system for speedy data acquisition. The pressure port locations in terms of x and y co-ordinates are given in tables 2a and 2b. Pressure port locations are also shown on the surface of the airfoil in figure 5. End plates were used at both ends of the model to eliminate the tip effect and to ensure 2-dimensional flow at the centre of the 2-D model.

For the wake survey a multi-port rake covering the entire width of the tunnel was used. Wake survey rake consisted of 96 pressure ports (91 total pressure ports and 5 static pressure ports). This rake was mounted horizontally near the mid-span at a distance of two chords from the airfoil trailing edge. The thickness of the rake was kept just enough to house the pressure scanners. The total pressure sensing was done using steel tubes of sufficient stiffness and length to ensure that the upstream influence of the rake body does not alter the measurement.

2.5 Instrumentation

The instruments used in the experiments are highly sophisticated and most advanced ones with which NWTF is equipped. All these instruments are actuated and controlled by Virtual Instruments. Software routines for VI's were developed in LabVIEW, which are described in Chapter 3.

2.5.1 Electronic Pressure Scanners

Electronic Pressure Scanners are differential pressure measurement units housing an array of piezo-resistive sensors, one for each pressure port. Each scanner has 32 ports. Each port consists of a wheatstone bridge diffused onto a single silicon crystal. Along with extreme resistance to over pressure, its linearity, hysterisis and repeatability are limited to less than 0.05% full scale. Scanners have two-position manifold, one is run mode and another is cal mode. The manifold position can be changed by applying a momentary pulse of control pressure. Run mode is used to acquire a pressure data and cal mode is used for calibration of pressure ports. When placed in calibration position all sensors are connected to a common calibration pressure port. The accuracy of the scanners is maintained within 0.05% of full scale pressure range through their periodic on-line calibration. The frequency of calibration is dependent on ambient conditions and it changes with time. A calibration performed immediately before a set of data is acquired assures the highest accuracy of the scanners.

The voltage output from the pressure sensors are connected to digitally addressed analog multiplexers at rates up to 20,000 Hz. Each sensors output is

selectively routed to the onboard instrumentation amplifier by applying its unique binary address to the multiplexers.

The multiplexed and amplified analog output of the scanner is capable of driving long lengths (up to 30fts) of cable to the remote A/D converter of DAQ board. Scanners require ±12V DC power supply for the operation of built-in analog/digital devices and a +5V DC power supply as the excitation voltage source for the sensors.

2.5.2 Digital Interface and Line Driver (DILD) Unit for ESP Scanners

The DAQ board provides 5-volts (TTL) logic level signals through its digital I/O lines, whereas the pressure scanners require 12-Volt (CMOS) logic level signals for binary addressing. Thus, there is a logic (TTL-CMOS) level mismatch between the DAQ board and scanners. The logic level shifters of the DILD unit compensates for this logic level mismatch. The DILD unit also provides digital fanout to drive 8 pressure scanners, and long cable (30 ft) drive capability. The regulated DC power supplies (±12V and ±5V) required for the operation of pressure scanners are also supplied by this unit.

2.5.3 Data Acquisition Board

A high speed Data Acquisition Board (DAQ Board) PCI-6034E with a sampling rate of 100K samples/s from National Instruments was used for data acquisition, which acts as an interface between the sensors and the computer. The data were acquired, digitized and transferred to the Virtual Instrument software routine by the DAQ board. The ADC has 16 bit resolution. With this board it is possible to scan 16 analog input channels at a maximum scan rate of 16 kHz. It has two 12-bit analog output channels, 8 digital I/O lines and two 24 bit counters.

2.6 Testing Configurations

The two-element airfoil model was tested in retracted configuration and in three different overhang configurations at a fixed gap over the angle of attack range of -10^0 to 30^0 in steps of 3^0. The retracted configuration provided the baseline data. The

three overhang positions for the flap were +5.23%, 0%, and -1.3%. The flap deflections for each overhang were 20^0, 25^0, and 30^0. All the flap deflections were not possible for the negative overhang because of mechanical restriction on the model.

2.7 Accuracy of Measurement

For the aerofoil surface pressure measurement pressure scanners of 20 inches of water column differential pressure measuring capability were used. Accuracy of differential pressure measurement for this scanner is within 2.5 Pascal, which corresponds to 0.05% of the scanner range.

For 30 m/sec wind speed and pressure coefficient of -12.0, the surface pressure value is about 6480 Pascal which is beyond the range of the scanner (± 5000 Pascal). Hence two scanners were used in a manner that for higher range of pressure the scanner reference is raised by connecting it to a known pressure which is already measured by using another scanner referenced to atmosphere. Maximum pressure on the lower surface of the main element is within the scanner range, so the reference for lower surface scanner is atmosphere. The accuracy of measurement for this scanner is within 2.5 Pascal. Maximum pressure on the upper surface of main element is above the range of scanner. So with reference to atmosphere the accuracy of measurement is within 5 Pascal. For flap, maximum surface pressure is within the range of the scanner, so the reference is atmosphere and accuracy of measurement is within 2.5 Pascal.

Tunnel dynamic pressure is measured by using a secondary standard digital manometer. This manometer uses differential pressure sensors of 7000 Pascal range having an accuracy of 3.5 Pascal, which is 0.05% of full scale range. The measurement accuracy at 30 m/s wind speed corresponding to dynamic pressure of 540 Pascal is within 0.64%.

For the wake measurement, scanners with 20 inches water column range were used for the outer wake region and a 10 inches water column range scanner was used for the center wake region. Total pressure measurement error inside the wake region is 0.23% while outside the wake region it is 0.46% at 30 m/sec.

three overhang positions for the flap were +5.23%, 0%, and -1.3%. The flap deflections for each overhang were 20^0, 25^0, and 30^0. All the flap deflections were not possible for the negative overhang because of mechanical restriction on the model.

2.7 Accuracy of Measurement

For the aerofoil surface pressure measurement pressure scanners of 20 inches of water column differential pressure measuring capability were used. Accuracy of differential pressure measurement for this scanner is within 2.5 Pascal, which corresponds to 0.05% of the scanner range.

For 30 m/sec wind speed and pressure coefficient of -12.0, the surface pressure value is about 6480 Pascal which is beyond the range of the scanner ($\pm$ 5000 Pascal). Hence two scanners were used in a manner that for higher range of pressure the scanner reference is raised by connecting it to a known pressure which is already measured by using another scanner referenced to atmosphere. Maximum pressure on the lower surface of the main element is within the scanner range, so the reference for lower surface scanner is atmosphere. The accuracy of measurement for this scanner is within 2.5 Pascal. Maximum pressure on the upper surface of main element is above the range of scanner. So with reference to atmosphere the accuracy of measurement is within 5 Pascal. For flap, maximum surface pressure is within the range of the scanner, so the reference is atmosphere and accuracy of measurement is within 2.5 Pascal.

Tunnel dynamic pressure is measured by using a secondary standard digital manometer. This manometer uses differential pressure sensors of 7000 Pascal range having an accuracy of 3.5 Pascal, which is 0.05% of full scale range. The measurement accuracy at 30 m/s wind speed corresponding to dynamic pressure of 540 Pascal is within 0.64%.

For the wake measurement, scanners with 20 inches water column range were used for the outer wake region and a 10 inches water column range scanner was used for the center wake region. Total pressure measurement error inside the wake region is 0.23% while outside the wake region it is 0.46% at 30 m/sec.

2.8 Pressure Measurement System

National Wind Tunnel Facility (NWTF), IIT Kanpur is equipped with a Virtual Instrument (VI) based eight channel pressure measurement system (see figure 6a). The system mainly consists of system hardware, which includes eight 32-port miniature pressure scanners and a digital interface and line driver (DILD) unit, and a VI-based data acquisition (DAQ) system. First three channels of the system are connected to the scanners installed inside the two-element aerofoil model (two in the main element and one in the flap) for its surface pressure data acquisition and next three are connected to the scanners installed inside the horizontal pressure rake which is mounted behind the model for wake survey. The accuracy of the measurement is maintained within $\pm 0.05\%$ of the full-scale (FS) pressure range through periodic on-line calibration of the pressure scanners.

The entire measurement chain is automated with VI-based application software using National instruments **Laboratory Virtual Instruments Engineering Workbench (Lab VIEW)** software. The VI-based DAQ system consists of a windows-based host computer equipped with a high-speed 16-bit DAQ board (PCI-6034E) and the VI based application software. The Application software links the host computer to the sensors of the scanners through DAQ board and the DILD unit and sends digital address to pressure scanners to select the sensors and acquires data through analog input lines of the DAQ board.

The motion control system has been integrated with the VI-based pressure measurement system for the aerofoil model testing. The 2D-aerofoil model is mounted in the upstream test section (UST) equipped with a motion controlled dual turn table system. The turn tables are mounted with their axes aligned vertically on the top and the bottom surfaces of the test section. These are provided with synchronous motion control, and are also capable of independent motion. The turntables can be positioned by the computer-controlled motion control system at any angular orientation with a fine resolution of 0.02^0.

3 - DATE ACQUISITION AND ANALYSIS

During the experiment as wind flows over the model, the model is subjected to aerodynamic forces. These forces are estimated from the pressures, measured using pressure scanner, on the airfoil and in the wake. Pressure scanners are connected to the pressure ports on the model through the PVC tubes. Pressure scanners emit electric signals of volt range. These signals are taken to the signal conditioner where they are amplified and filtered. The conditioned signals are acquired by the DAQ Board, which resides inside the computer. The ADC in the DAQ board digitizes the data and provides to the program as input. This digital information is analyzed by the program and presented in the graphs in an intelligible form. The raw data is kept in a text file and is analyzed later to obtain the coefficients of lift, drag and, pitching moment about leading edge. Data acquisition is performed by the PCI-6034E DAQ board. For controlling the DAQ board and analyzing the data to present the results, programs are developed in LabVIEW software.

3.1 LabVIEW

LabVIEW (Laboratory Virtual Instrument Engineering Workbench) is a program development environment, which uses graphical language, G, to create programs which are analogous to the programs developed in some other environments like C, BASIC, and FORTRAN. But unlike these programming environments, in which programs are written in text form, LabVIEW supports the program in block diagram form. It uses terminology, icons and ideas to describe programming actions. In the program, a function executes only after the data is received by all of its input terminals. This is the data-flow principle, which governs the execution of the program in a straight forward manner. It comprises extensive libraries of functions for performing various programming tasks. It includes libraries for data acquisition, VXI, GPIB and serial port instrumentation control, data analysis, data presentation and data storage. It also includes conventional programming development tools, so that one can set breakpoints, animate program execution to see how data passes through the program to make debugging and program development easier.

3.2 Data acquisition

Data acquisition is performed using the PCI-6034E DAQ board. Voltage signals from the pressure scanners, after passing through the DILD unit (this unit compensates the logic level mismatch between the pressure scanner and DAQ board), is received by ADC. Voltage signals represent varying pressure on the surface of the airfoil and in the wake. Voltage data from the six channels (six pressure scanners) and the excitation from the 7th channel are collected. This voltage data is normalized with respect to the excitation voltage. This normalized raw data (V/V) along with the angle of attack and dynamic head, is stored in a text file. At the start of the experiment no wind data is collected at 0^0 angle of attack. Front panel of the data acquisition program used in the present experiments is shown in figure 6b.

3.3 Data analysis

No wind data is subtracted from the wind data and the resulting data is analyzed. This raw data (in volts) is converted into pressure data by using scanners calibration constants. With this pressure data, pressure distribution over the airfoil is plotted at each angle of attack. From the pressure distribution on the airfoil lift and pitching moment are calculated. The drag on the airfoil is calculated from the wake profile drag. Calculation of lift, drag, and pitching moment is explained below.

3.4 Calculation of drag, lift, and pitching moment

Wake survey system is used to compute drag on the airfoil. To accurately measure wake profile more number of pressure ports are provided in the center of the wake. Wake rake system is fixed perpendicular to the plane of the wing and two-chord behind the airfoil trailing edge.

For flow past an object, there is a loss of momentum as a part of the fluid passes over the model. This momentum loss gives the profile drag. Calculation of drag is given below,

$$D = \frac{mass}{sec} \times change\ in\ velocity$$

$$D = \iint \rho \, U \, dS \, (U_\infty - U)$$

dS = the small area of wake perpendicular to the airstream

$$\text{Drag coeffient} = C_d = \frac{D}{\frac{1}{2}\rho U_\infty^2 S}$$

$$C_d = 2\iint \left(\frac{U}{U_\infty} - \frac{U^2}{U_\infty^2} \right) \frac{dS}{S}.$$

With $S = C \times 1$ and the area $dS = dy \times 1$ for unit span of the airfoil, the above equation may be written as

$$C_d = 2\int \frac{U}{U_\infty} \left(1 - \frac{U}{U_\infty} \right) \frac{dy}{c}.$$

Here the x-coordinate is along the chord and the y-coordinate is perpendicular to the chord. Static pressure ports are located at different y - locations on wake survey rake. The average static pressure is extracted and this is subtracted from each of the total pressures at different y–locations to get the dynamic head. Wake profile is plotted as U/U_∞ vs. y - locations of total pressure ports. By using the above equation drag was computed.

Lift on the airfoil was calculated by integrating the static pressures over the model surface. Surface pressure measurements were done with 85 pressure ports along the chord at mid span of the model. Integration of the surface pressure distribution yielded normal force N, perpendicular to the chord, and axial force A, along the chord. Lift was then calculated from the normal and axial forces. Equations used for the calculations are given below for unit span of the airfoil.

$$C_N = \frac{N}{Q_\infty C} = -\frac{1}{C}\int (C_{PU} - C_{PL})dx$$

$$C_A = \frac{A}{Q_\infty C} = -\frac{1}{C}\int (C_{PU} - C_{PL})dy$$

$$C_l = C_n \cos\alpha - C_A \sin\alpha$$

For flap deflected configurations total lift is the sum of the lift produced by the main element and the flap. Lift calculation for flap deflected configurations is given below

$$\text{Lift} = \frac{1}{2} \rho U_\infty^2 C C_l$$

$$C_l = \left(C_{N\,m} + C_{N\,f} \cos \delta_f\right)\cos \alpha - \left(C_{A\,m} + C_{A\,f} \cos \delta_f\right)\sin \alpha$$

Pitching moment can be calculated from the pressure distribution on the surface of the airfoil. Pitching moment calculations for retracted configuration and for flap deflected configurations are described below. For retracted configuration, pitching moment about the leading edge has contribution from both normal and axial forces. Contribution from the normal force is given by

$$C_{mn} = \frac{1}{C} \int (C_{pu} - C_{pl})\left(\frac{x}{C}\right) dC \; .$$

Contribution from the axial force is given by

$$C_{ma} = \frac{1}{C} \int (C_{pu} - C_{pl})\left(\frac{y}{C}\right) dC$$

where, x and y are the distances from the leading edge. Total pitching moment about the leading edge is the sum of these two moments,

$$C_{mle} = C_{mn} + C_{ma}$$

For flap deflected configurations, the moment from flap is also to be considered in addition to the main element moment. Thus, the total pitching moment is the sum of the moment due to main element and the flap. Calculation of moment due to main element is same as the retracted configuration. Moment from flap has two contributions; one from normal force and another from axial force on the flap. Calculations of these moment contributions from normal and axial forces on the flap are described below.

Moment about the leading edge of the main element due to the axial force on the flap is

$$C_{maf} = C_{Af} \times \frac{d_1}{C}$$

where C_{Af} is the axial force coefficient calculated by integrating the pressure force along the chord and d_1 is the perpendicular distance from the leading edge of the main element to the chord line of the flap.

Moment about the leading edge of the main element due to the normal force on the flap is

$$C_{mnf} = C_{Nf} \times \frac{d_2}{C}$$

where C_{nf} is the normal force coefficient of the flap and d_2 is the perpendicular distance between the leading edge of the main element and the perpendicular line to the flap chord passing through the flap normal force location. The location of the normal force acting on the flap chord is found by dividing the moment about the leading edge of the flap with flap normal force.

The total pitching moment about the leading edge of main element for flap deflected configurations is, therefore, given by

$$C_{mlef} = C_{mnf} + C_{maf}$$
$$C_{mlem} = C_{mnm} + C_{mam}$$
$$C_{mle} = C_{mlem} + C_{mlef}$$
$$M_{lef} = \frac{1}{2}\rho u_\infty^2 C^2 C_{mle}$$

4 - RESULTS AND DISCUSSION

Experiments were conducted on a two-element airfoil in static conditions at a constant wind speed of 30m/s, which corresponds to a chord Reynolds number of 1.53×10^6. The airfoil model was mounted vertically on the turntable. Turntable rotation provided the various angles of attack. Experiments were conducted to obtain pressure distribution on the airfoil surface and wake profile behind the airfoil for angles of attack -10^0 to 30^0. The pressure data on the airfoil surface and in the wake were used to estimate the sectional properties, lift, drag and pitching moment coefficients, of the airfoil. Results of this experimental investigation for retracted and flap deflected configurations at different overhang positions are presented below.

4.1 Retracted configuration

Model was mounted in retracted position (see figure 4a) and tested for angles of attack -6^0 to 30^0 with intermediate angles of attack. Model was also tested at different turntable speeds (4, 8, 12, and 16 rpm) to study the effect of turntable speed on the aerodynamic coefficients and on hysteresis effect. Results of these tests in the form surface pressure distribution and wake profile for various angles of attack are discussed below followed by a discussion on aerodynamic characteristics.

4.1.1 Surface pressure distribution and wake profile

Surface pressure distributions on the airfoil for selected angles of attack are shown in figures 7a and 7b. Pressure distributions indicate that the change in Cp is dominant on the upper surface than the lower surface as the angle of attack increases. The flow on the upper surface accelerates more rapidly than the lower surface of the airfoil, because of the camber of the airfoil. This lowers the local static pressure on the upper surface. The suction side minimum pressure coefficient at angle of attack 25^0 is -9. As the angle of attack is increased beyond this α, the flow is separated and stall is observed. Once the airfoil is stalled the pressure on the upper surface is nearly constant which is expected in the separated flows. From the pressure distribution, as shown in the figures 7a and 7b, flow separation point can be approximately identified on the airfoil surface.

For a flow past an airfoil, the part of the air that passes over the model suffers a loss of momentum and this loss is the profile drag of the airfoil. Dimensionless velocity profiles (U/U_{inf}) in the wake at different angles of attack are presented in figures 8a and 8b. As the angle of attack increases the size of the wake increases slowly and shifts to the right (as seen from the wind direction). At the stall wake size increases suddenly, as seen from the figures 8a and 8b, due to the flow separation on the airfoil.

4.1.2 Aerodynamic characteristics

Sectional properties of the airfoil are shown in figures 9a to 9c. In figure 9a, lift coefficient is plotted against angle of attack. As expected, C_l increases almost linearly for smaller angles of attack. The maximum value of C_l is observed to be about 1.24 at $\alpha = 25^0$. A slight increase in angle of attack beyond 25^0 causes flow separation and the airfoil stalls. At this stage C_l drops abruptly from 1.24 to 0.95 for 1^0 increment in angle of attack.

Figure 9b shows the variation of drag coefficient with angle of attack. As seen from the figure 9b the drag coefficient is almost constant upto $\alpha =10^0$; it increases slowly up to 25^0 to a value of 0.03. After that as the airfoil stalls, C_d increases suddenly from 0.03 to 0.22 for 1^0 increment in angle of attack. Wake size, as seen in figures 8a and 8b, for $\alpha= 25^0$ and $\alpha= 26^0$ gives an idea about the drag and it is much wider for $\alpha= 26^0$.

Pitching moments about the leading edge and 0.2C of the airfoil are plotted in figure 9c. As seen from the figure, the pitching moment about the leading edge decreases almost linearly upto $\alpha = 25^0$. The pitching moment about the 0.2C is almost constant indicating that the aerodynamic center of the airfoil is close to 0.2C for this retracted configuration. After the stall due to flow separation on the airfoil, normal force developed by the airfoil is decreased and non-linear behavior in pitching moment is observed. Negative slope observed in the pitching moment curve is especially important since negative slope gives the stability.

4.1.3 Hysteresis effect

Wind-Tunnel studies of airfoil performance are of great importance for designing and building aircraft. Study of hysteresis effect in aerodynamic performance of airfoil is important since it is not desirable. Hysteresis has been considered as a low Reynolds number phenomenon, occurring in post stall recovery of single element airfoils. However, the present tests reveal that even at a relatively high Reynolds number, hysteresis still affects the results of wind-tunnel testing.

For surface pressure measurement over the airfoil, the model was set to 0^0 angle of attack at the wind-off condition and then wind speed was increased to the test Reynolds number. Once the tunnel speed stabilized, the angle of attack was decreased to -6^0 and then increased to 30^0 and then decreased to 0^0 in steps of 2^0 or 3^0 without stopping the tunnel, while acquiring pressure data at the required angles of attack. For increasing angle of attack stall occurs at $\alpha=25^0$ while decreasing angle of attack stall occurs at $\alpha=22^0$. Hysteresis loop has been observed in the aerodynamic characteristics for $22^0 < \alpha < 27^0$. It can be seen from the C_{l}, C_d and C_m curves as shown in 9a, 9b, and 9c. The hysteresis loop in the drag and pitching moment curves has the same range of angle of attack as in the lift curve. Hysteresis effect is also seen in the pressure data at the various pressure ports on the surface of the airfoil as shown in figures 10. Effect of hysteresis in the flow on the upper surface of the airfoil is reduced towards the trailing edge. On the lower surface of airfoil the hysteresis in the flow is less significant compared to the upper surface.

Wind tunnel testing of GA(W) airfoil in retracted configuration, Biber and Zumwalt (1993) did not observe hysteresis in the aerodynamic characteristics at Reynolds number 2.2×10^6. But at lower Reynolds number (Re=250,000), Hoffmann (1991) and at Reynolds numbers 70,000 to 300,000 Marchman (1985) have reported hysteresis loop near the stall region. However, present test at Re=1.53×10^6 shows the hysteresis loop near the stall region. Similar results at Re $=10^6$ were also reported by Mittal and Saxena (2002) in their study on NACA 0012 airfoil.

It appears from the surface pressure distribution (figures 7a and 7b) that the movement of separation point towards leading edge during pitch-up mode is slower

than the movement towards trailing edge during pitch-down mode. This is probably responsible for hysteresis in the sectional properties near the stall angles. For the same angle of attack, in the hysteresis loop, airfoil develops lower lift and higher drag with the decreasing angle of attack as compared to lift and drag developed with increasing angle of attack.

Model was also tested at different turntable speeds 4, 8, 12 and 16 rpm, but as the data were acquired in step and pause mode during these tests there is no discernible effect of the turntable speed on aerodynamic coefficients and on hysteresis loop. Lift and drag coefficients graphs for these tests are shown in figures 11a & 11b for different turntable speeds.

4.2 Flap deflected configurations

All the flap deflected configurations were tested at a fixed gap of 2.61% for three overhangs 5.23%, 0%, -1.3% at a chord Reynolds number of 1.53×10^6. Results of these tests are discussed in the following sections.

4.2.1 Effect of flap deflection at zero overhang

For this portion of the study, experiments were conducted at three flap deflections 20^0, 25^0 and 30^0 at 0% overhang.

4.2.1.1 Surface pressure distribution and wake profile

Surface pressure distributions are shown in figures12a and 12b for three flap deflections at different angles of attack. The main element surface pressure distribution is similar for three flap deflections up to angle of attack 22^0. But on the flap, lower values of pressure coefficient are observed with increased flap deflection. At $\alpha = 24^0$ surface pressure distribution is different both on the main element and flap. This is because at this angle of attack the flow is separated for 25^0 and 30^0 flap deflections but the flow remained attached for flap deflection 20^0. After $\alpha = 24^0$, the flow separation and stall were observed for all the cases. This is shown in figure 12b. Thus, the effect of flap deflection on overhang is that the stall will occur early with increase in flap deflection.

Wake profiles for zero overhang are shown in figures 13a to 13c. As seen from figure 13a, flow at lower angles of attack is completely attached and the wake is smaller. At larger angles of attack, as seen from figure 13b, wakes of both main and flap elements are clearly visible separately for flap deflected configurations as against only one wake seen in retracted configuration. The two separate wakes of the main and flap elements are visible until the airfoil stalls. After stall, as the flow on the airfoil separates, wakes of the main element and flap merge into a single wider wake. This is observed at $\alpha = 25^0$ from figure 13c. As the flap deflection is increased from 20^0 to 25^0 wake size increases slightly, but for 30^0 flap deflection a wider wake is observed for the same angle of attack. Thus, the effect of increase in flap deflection causes flow to be more susceptible to separation at early angles of attack as the effective angle of attack of the airfoil is increased.

4.2.1.2 Aerodynamic characteristics

The aerodynamic sectional properties for flap deflected configurations at zero overhang are presented in figures 14a to 14c. As seen from the figure 14a, lift coefficient increases with increase in flap deflection at a fixed angle of attack. Also, the stall occurs earlier with increase in flap deflection. This is expected since effective angle of attack is increased with increase in flap deflection. Flap deflection increases the C_{lmax} by shifting the lift curve upwards. As seen from figure 14b, it also increases drag with increase in flap deflection. Thus, flap deflection is a compromise of high lift, low drag and stall angle. Pitching moment coefficient about the leading edge is shown in figure 14c. Flap deflection shifts the pitching moment curve upwards. Flow at lower angles of attack over the flap is affected by the wake of main element due to this the normal force experienced by the flap is somewhat lower than that in the retracted case. That is why at lower angles of attack the moment curve is deviated slightly. This is also seen in lift curve at lower angles of attack.

4.2.2 Effect of flap deflection on +5.23% overhang

To study the effect of flap deflection on positive overhang, flap was set at 5.23% overhang and the airfoil was tested for three flap deflections 20^0, 25^0, and 30^0.

4.2.2.1 Surface pressure distribution and Wake profile

Surface pressure distributions for the main element and the flap for the positive overhang cases are shown in figures 15a and 15b. Main-element lower surface pressure distribution near the trailing edge gets affected due the positive overhang and the flow is accelerated in the gap causing decrease in pressure. This can be seen clearly near the lower surface pressure distribution of the main element near the trailing edge from figures 15a and 15b. The pressure distribution on the main element is almost similar for three flap deflections up to $\alpha = 22^0$. As the angle of attack is increased further, higher flap deflection causes flow separation earlier. This is observed in figure 15b. As seen from figures 12b and 15b for zero and positive overhangs, respectively, for $\alpha = 24^0$, the airfoil with 25^0 and 30^0 flap deflections at zero overhang stalls; but at positive overhang of 5.23% flow separation occurs only for 30^0 flap deflection. Thus, it can be argued that the positive overhang delays flow separation on the airfoil.

Wake profiles for the present case are shown in figures 16a to 16c. As seen from figure 16a, for smaller angle of attack, the wake is narrow, but its size increases as the flap deflection increases from 20^0 to 30^0 although the flow is completely attached to the airfoil surface. At higher angles of attack wakes of both main element and flap are visible in the figure 16b similar to those observed in figure 13b. As the angle of attack is increased further, wakes merge into a single wider wake due flow separation. This happens first at $\alpha = 24^0$ for higher flap deflection of 30^0 as seen from figure 16c. At $\alpha = 25^0$, for all flap deflections wake merging is observed in figure 16c.

4.2.2.2 Aerodynamic characteristics

Aerodynamic coefficients for the positive overhang case are shown in figures 17a to 17c. Effect of flap deflection on lift coefficient for 5.23% overhang is shown in figure 17a. As seen from the figure17a, lift curve shifts upward as the flap deflection is increased from 20^0 to 30^0. Thus, flap deflection produces more lift at a given angle of attack as compared to the retracted configuration. But as the flap deflection is increased, the increase in lift gets smaller and smaller and after a certain flap angle flow on the flap gets separated and the lift benefit from the flap disappears. Effect of

flap deflection on drag curve for overhang 5.23% is shown in figure17b. Drag produced by the flap deflected configurations increases with increase in flap deflection. Drag curve shifts upward with flap deflection. Increase in flap deflection gives high lift, but at the same time increases drag and stall occurs earlier. Effect of flap deflection on pitching moment about leading edge for 5.23% overhang is shown in figure 17c. At lower angles of attack, pitching moment variation is not linear. It appears that the main element wake affecting the flow over flap for low angles of attack; due to this, normal force developed by the flap is decreased and its effect is propagated to the moment and lift coefficients. At higher angles of attack below the stall, the main element and the flap are having separate wakes.

4.2.3 Effect of overhang

To study the effect of overhang on the aerodynamic performance of the two-element airfoil, model was tested for positive overhang (5.23%), zero overhang and negative overhang (-1.3%) at different flap deflection 30^0 over a range of angle of attack -10^0 to 30^0. Surface pressure distributions on the main-element and flap are presented in figures 18a and 18b. As seen from the figures, the upper surface pressure distribution on the main element is almost same for all the three overhang positions upto $\alpha=22^0$. Pressure on the lower surface of the main-element is also almost same with exception of positive overhang at which near the trailing edge of main element shows negative pressure. For negative overhang, flow over the flap is mostly separated in at lower angles of attack.

The wake profiles of three different overhangs for 30^0 flap deflection are given in figures 19a to 19c. Negative overhang case shows the wider wake compared to positive and zero overhangs. Separate wake profiles for the main element and the flap are seen from the figure 19b. After $\alpha=22^0$, the wakes of the main element and the flap merges into a single wider wake due to flow separation (see figure 19c).

The aerodynamic coefficients, as presented in figure 20a, shows that as the overhang is changed from 5.23% to 0%, the lift curve is shifted upward; and when it is changed to negative overhang, the lift curve shifted downward. It is also seen from figure 20a that the lift is maximum for zero overhang and is lower for both positive

and negative overhangs. Maximum values of lift coefficient at each overhang for different flap deflections are given in table 3.

The effect of overhang on drag coefficient is shown in figure 20b. As the overhang is changed from positive to 0%, the value of drag was not changed appreciably. But negative overhang effects drag significantly and the drag curve shifts upward as the flow on the flap is separated at early angles of attack. Lin and Dominick (1997) have also observed separation for negative overhang cases.

Pitching moment about the leading edge of main element is shown in figure 20c. Pitching moment curve shifts upward for positive and negative overhangs as compared with 0% overhang.

4.2.4 Hysteresis effect

For studying the hysteresis effect on the aerodynamic characteristics for flap deflected configurations, tests were carried out the same way as the retracted configuration. All flap deflected configurations show hysteresis effect on the aerodynamic characteristics. Hysteresis loop has been observed in the range of $20^0 < \alpha < 27^0$. This can be seen from the lift, drag and pitching moment coefficients curves for all flap deflected configurations in the figures 14, 17, and 20. Due to hysteresis the aerodynamic performance gain of the two-element airfoil by deflecting flap is reduced within the hysteresis loop. The flap deflected configuration has significant effect on the hysteresis loop and it is found to be wider than that of the retracted case. Similar observations are also made by Biber and Zumwalt (1993).

From the current investigation it appears that only surface pressure and wake survey measurement are not sufficient to fully understand the physics behind the hysteresis phenomena. Previous researchers, Marchman (1985), Biber and Zumwalt (1993) were also unable to explain fully the phenomenon of hysteresis. Detailed flow field survey and flow visualization are also needed to study the hysteresis effect.

5 - CONCLUSIONS

An experimental investigation was carried out on a two-element airfoil at a chord Reynolds number 1.53×10^6. The model was tested for retracted and flap deflected configurations to study the pressure distribution and aerodynamic characteristics using the surface pressure measurement on the airfoil and wake survey measurements. Various effects influencing the aerodynamic characteristics of two-element airfoil have been obtained. Main observations are summarized below.

1. Maximum lift coefficient for the retracted configuration of the present two-element airfoil is about 1.242 at an angle of attack 25^0 and corresponding drag coefficient is about 0.03. For the flap deflected configurations C_{lmax} is about 2.01 at an angle of attack of 25^0.

2. Flap deflection was found to increase lift, drag, and pitching moment about the leading edge and decreased the stall angle as compared with the retracted configuration. The lift curve shifted upward for flap deflected configurations. The stall was more severe for the flap deflected configurations.

3. Results of zero overhang showed increase in lift as compared with both positive and negative overhangs. Increasing trend is observed in drag and pitching moment coefficients for negative overhang as compared with positive and zero overhangs.

4. Flap retracted configuration showed significant hysteresis in the sectional properties as well in the surface pressure distribution during pitch-up and pitch-down modes near the stall. Results of flap deflected configurations also showed similar hysteresis effect in the sectional properties. The hysteresis loop was significantly increased due to flap deflection in the present investigation

5. It appears from the surface pressure distribution that the movement of separation point towards leading edge during pitch-up mode is slower than the movement towards trailing edge during pitch-down mode. This is responsible for hysteresis in the sectional properties near the stall angle.

FUTURE SCOPE

Effect of overhang and flap deflection on the aerodynamic performance of two-element airfoil at fixed gap has been studied at constant Reynolds number. Further research is proposed to study the variation of gap effect on the aerodynamic performance of the two-element airfoil. Hysteresis effect in the aerodynamic coefficients can be understood more clearly from the flow visualization on the airfoil near the stall angles of attack and also the effect of Reynolds number on the aerodynamic characteristics of two-element airfoil.

References

1. Adair, D., and Horne, W.C., "Turbulent Separated Flow over and Down Stream of Two-Element Airfoil," *Experiments in Fluids*, Vol. 7, No. 8, 1989, pp. 531-541.

2. Biber, K., and Zumwalt, G. W., "Hysteresis Effects on Wind Tunnel Measurements of a Two-Element Airfoil," *AIAA Journal*, Vol. 31, No. 2, 1993, pp. 326-330.

3. Biber, K., and Zumwalt, G. W., "Flow Field Measurements on Two-Element Airfoil with Large separation," *AIAA Journal*, Vol. 31, No. 3, 1993, pp. 459-464.

4. Daryl L.Bonhaus and W.Kyle Anderson, Dimitri J.Mavriplis, "Numerical Study to Assess Sulfur Hexafluoride as a Medium for Testing Multi-element Airfoil", NASA Technical Paper -3496, June 1995.

5. Jewel B.Barlow, William H.Rae, Jr., Alan Pope, *"Low-Speed Wind Tunnel Testing"*, Wiley, New York, 1999.

6. John A. Hoffmann., "Effect of Free Stream Turbulence on the performance Characteristics of an Airfoil," *AIAA Journal*, Vol. 29, No. 9, 1991, pp. 353-1354.

7. John C. Lin., and Chet J. Dominik, "Parametric Investigation of a High Lift Airfoil at High Reynolds Numbers," *Journal of Aircraft*, vol. 34 , No. 4, 1997, pp. 485-491.

8. Marchman III, J.F. and Abtahi, A.A., "Aerodynamics of Aspect Ratio 8 Wing at Low Reynolds Numbers", *Journal of Aircraft*, Vol. 22, No. 7,1985, pp. 628-634.

9. Meredith, P.T., "Viscous phenomena Affecting High-lift systems and suggestions for future CFD Development,"*AGARD-CP-515*, September 1993, pp.19.1-19.8.

10. Nakayama, A., Kreplin, H.P., and Morgan, H.L., "Experimental Investigation of Flow Field about a Multi-Element Airfoil," *AIAA Journal*, Vol. 28, No.1, 1990, pp.14-21.

11. Sanjay Mittal, Priyank Saxena, "Hysteresis in Flow Past a NACA 0012 Airfoil", *Computer methods in applied mechanics and engineering*, Vol. 191, Issues 19-20, 2002, pp. 2207-2217.

12. Smith, A. M. O., "High-Lift Aerodynamics," *Journal of Aircraft*, Vol.12, No. 6, 1975, pp. 501-530.

13. Stauart E. Rogers. , N. Lyn Wiltberger, Dochan Kwak, "Efficient Simulation of Incompressible Viscous Flow over Single and Multi-Element Airfoils." *Journal of Aircraft*, Vol. 30, No. 5, 1993, pp. 736-743.

14. Valarzo, W. O., Dominik, C.J., and Mc Ghee, R.J., Goodman, W.L., paschal, A.B., Multi Element Airfoil Optimization for Max Lift at High Reynolds Number", *AIAA Paper*, 91-3332-CP, 1991.

15. Valarzo, W. O., Dominik, C.J., and Mc Ghee, R.J., "Multi-Element Airfoil Performance due to Reynolds and Mack number Variation," *Journal of Aircraft*, Vol. 30, No. 5, 1993, pp. 689-694.
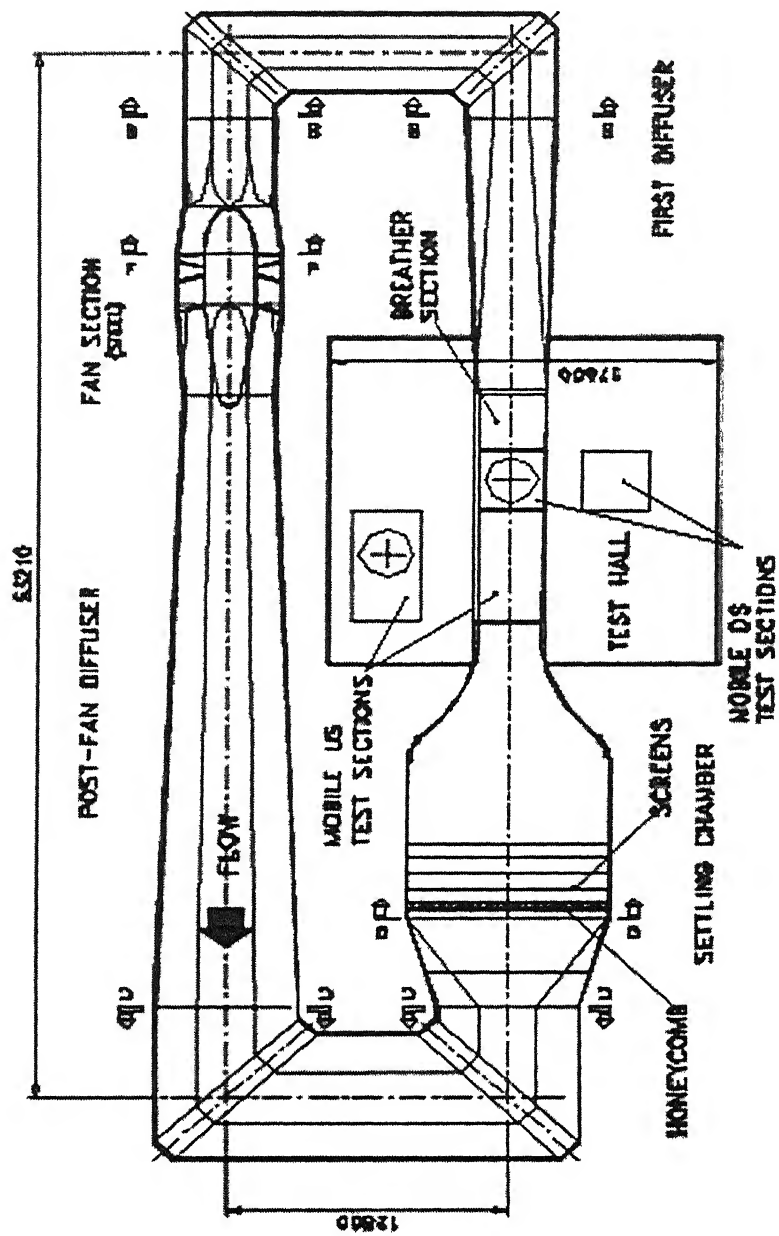
Figure 1: Aerodynamic layout of NWTF
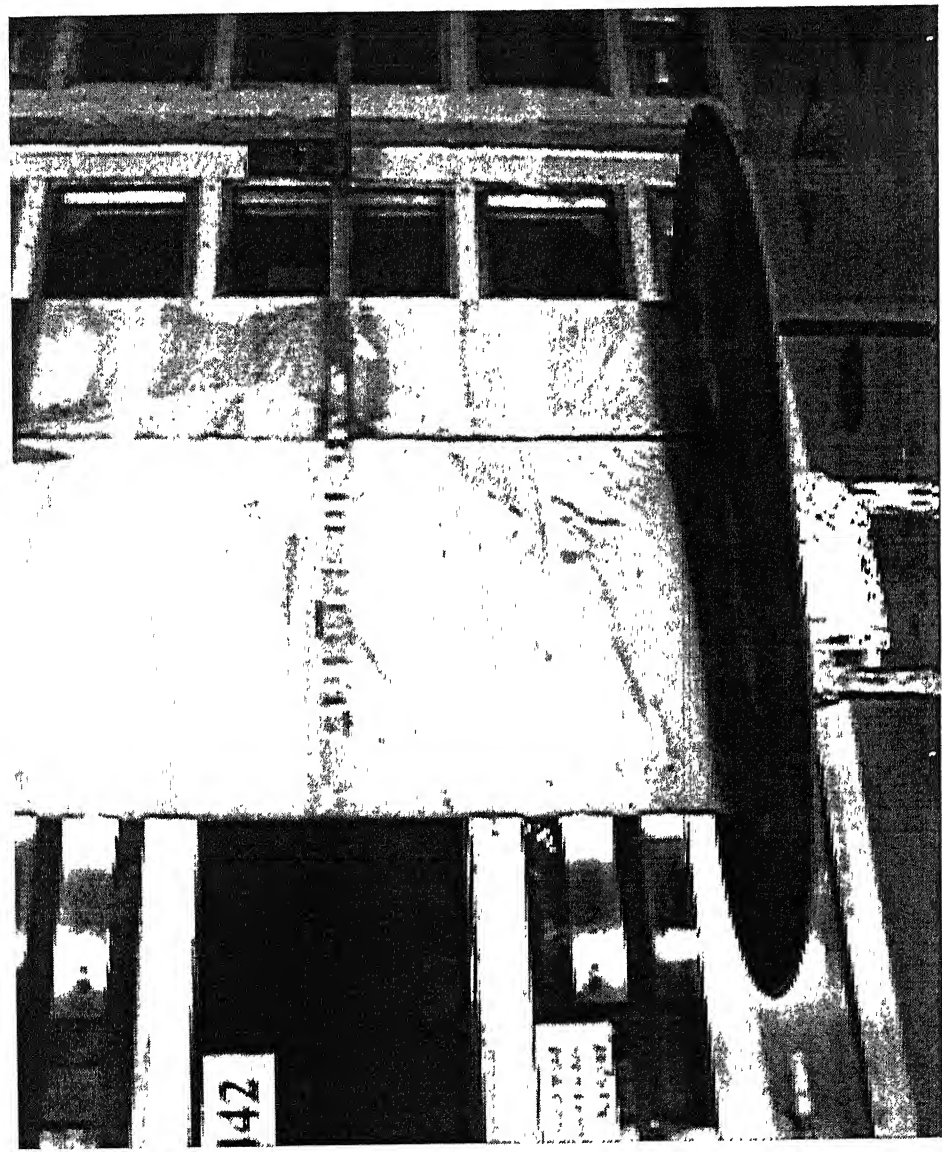
Figure 2a: Two-element airfoil model mounted in retracted position showing endplate and mounting bars.
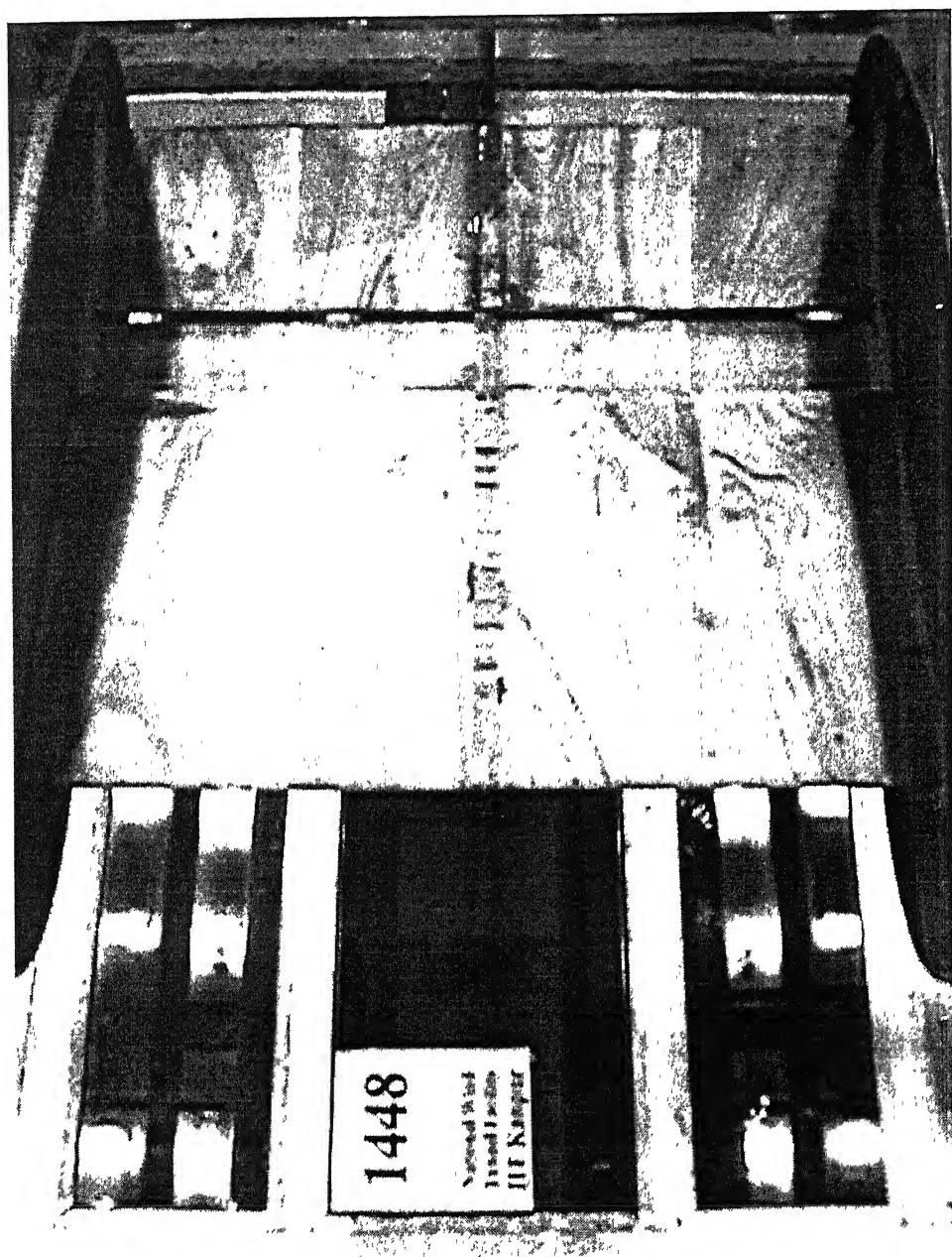
Figure 2b: Two-element airfoil model mounted in flap deflected position.
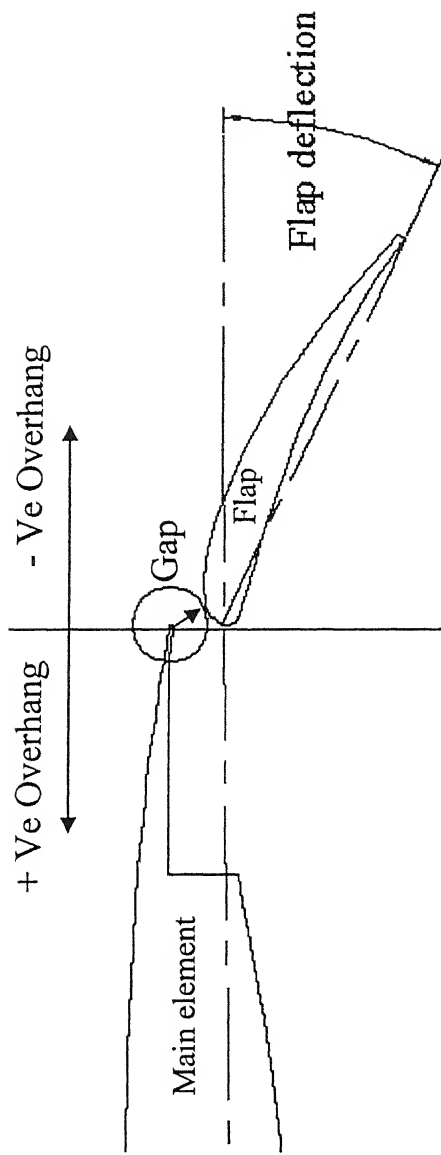
Figure 3: Definition of gap, overhang and flap deflection of a two-element airfoil.
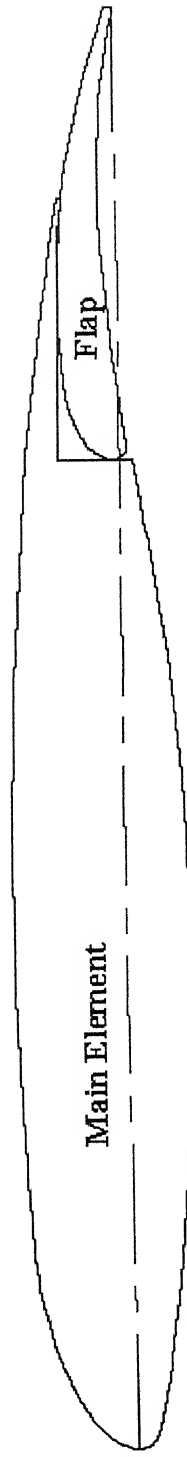
Figure 4a: Retracted configuration of the airfoil.
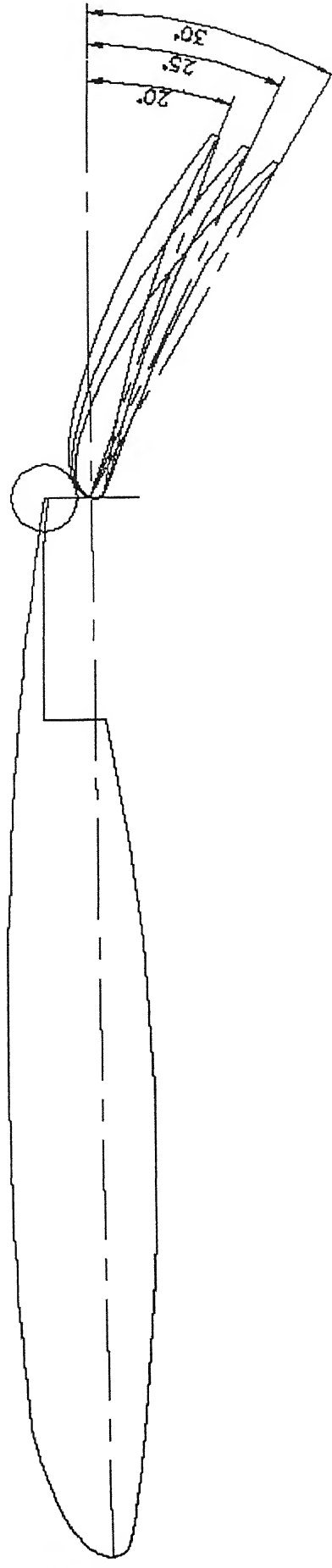
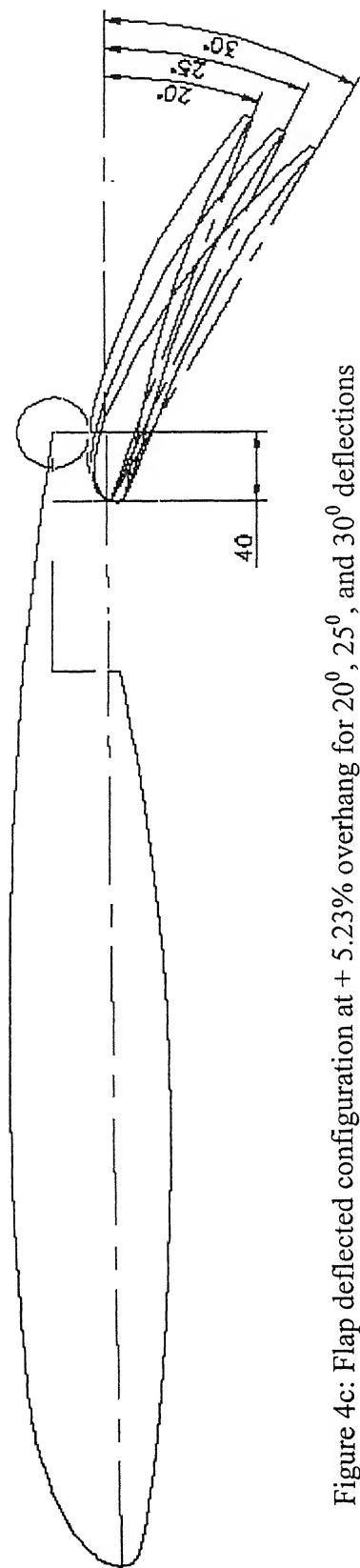Figure 4b: Flap deflected configuration at 0% overhang for 20^0, 25^0, and 30^0 flap deflections.

Figure 4c: Flap deflected configuration at + 5.23% overhang for 20^0, 25^0, and 30^0 deflections

Figure 4d: Flap deflected configuration at -2.61% overhang for 30^0 flap deflection.
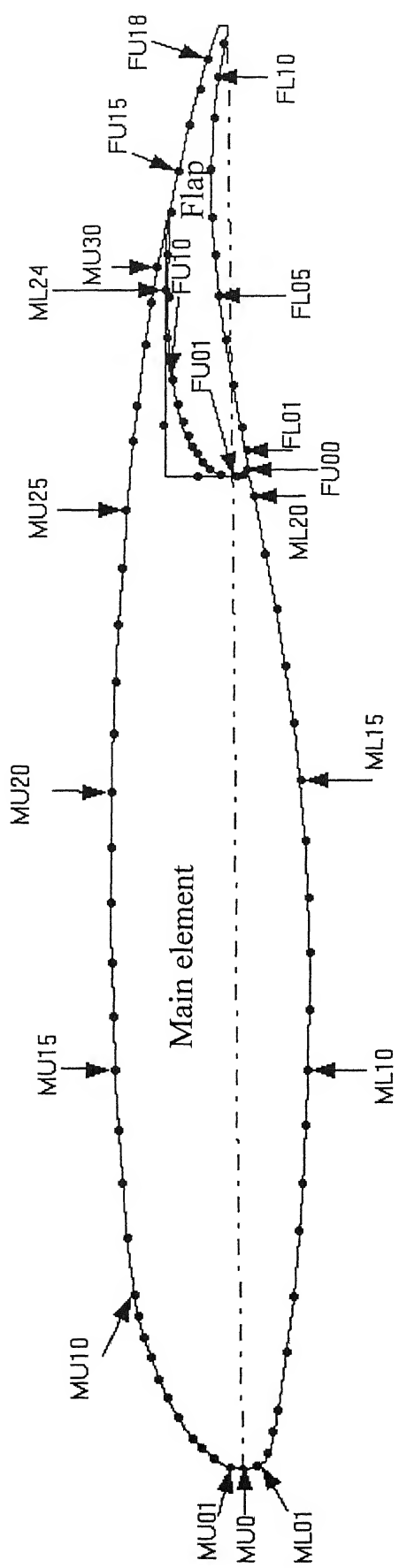
Figure 5: Pressure port locations on the two-element airfoil.
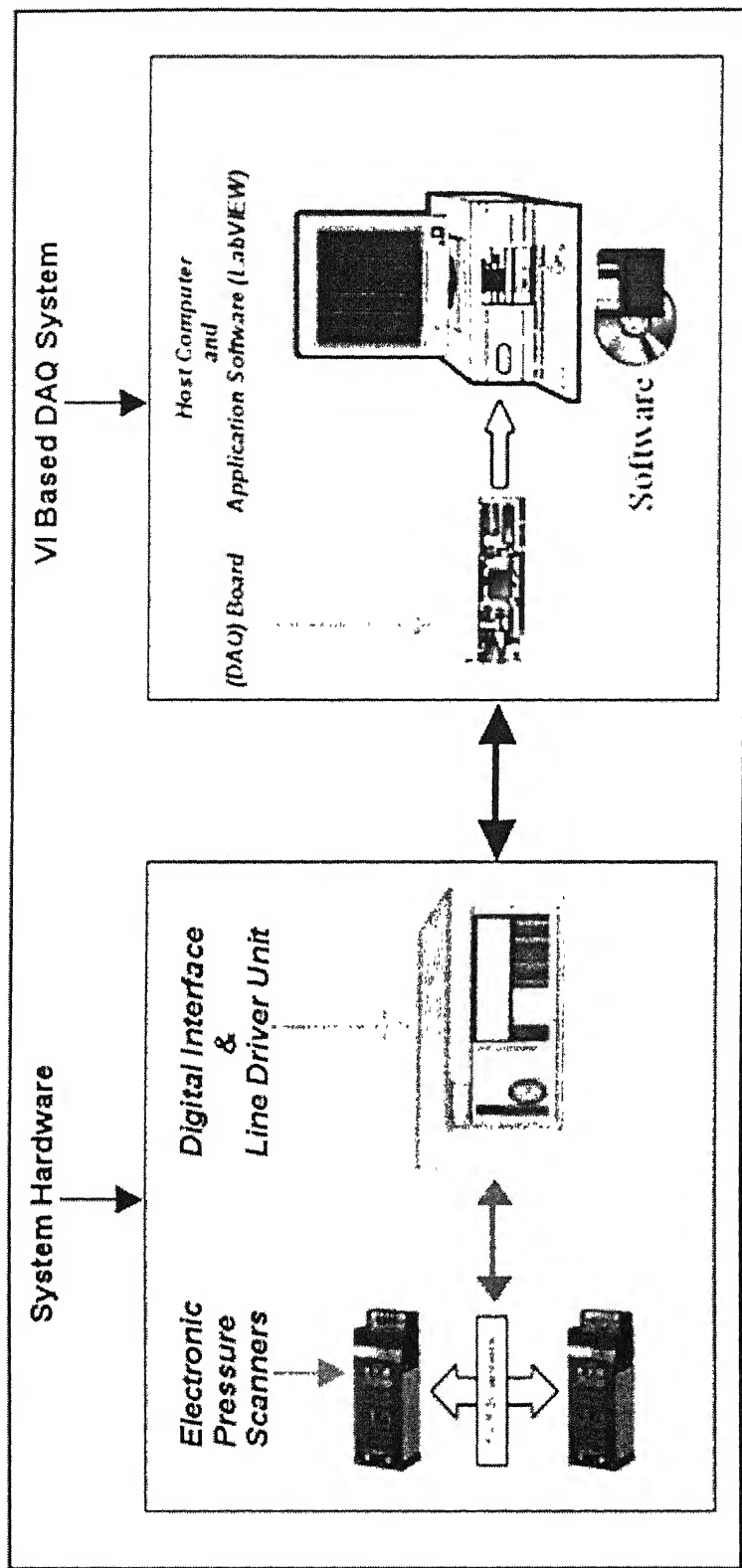
Figure 6a: VI Based 8-Channel Pressure Measurement System
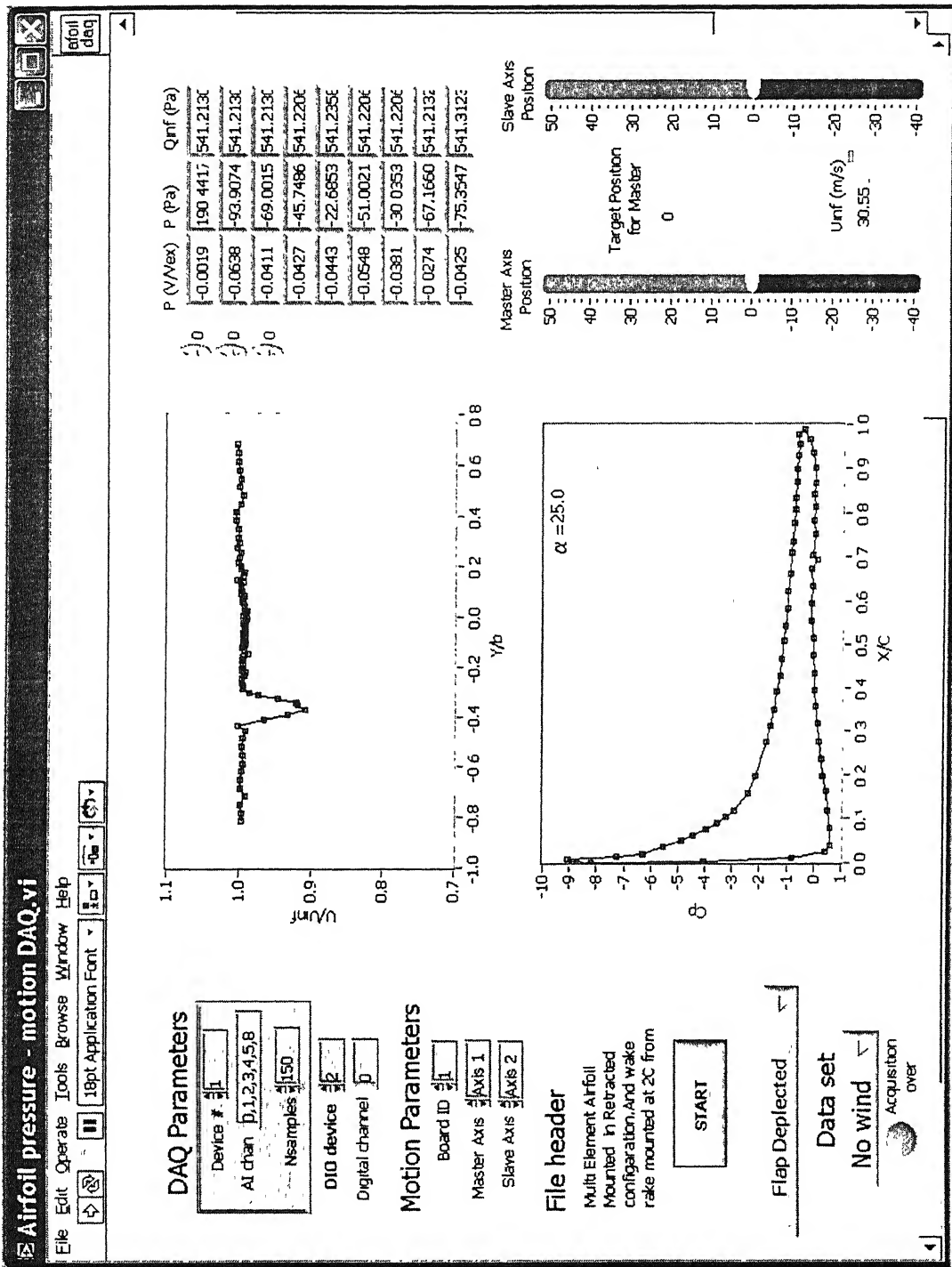
Figure 6b: Front panel of the data acquisition program.
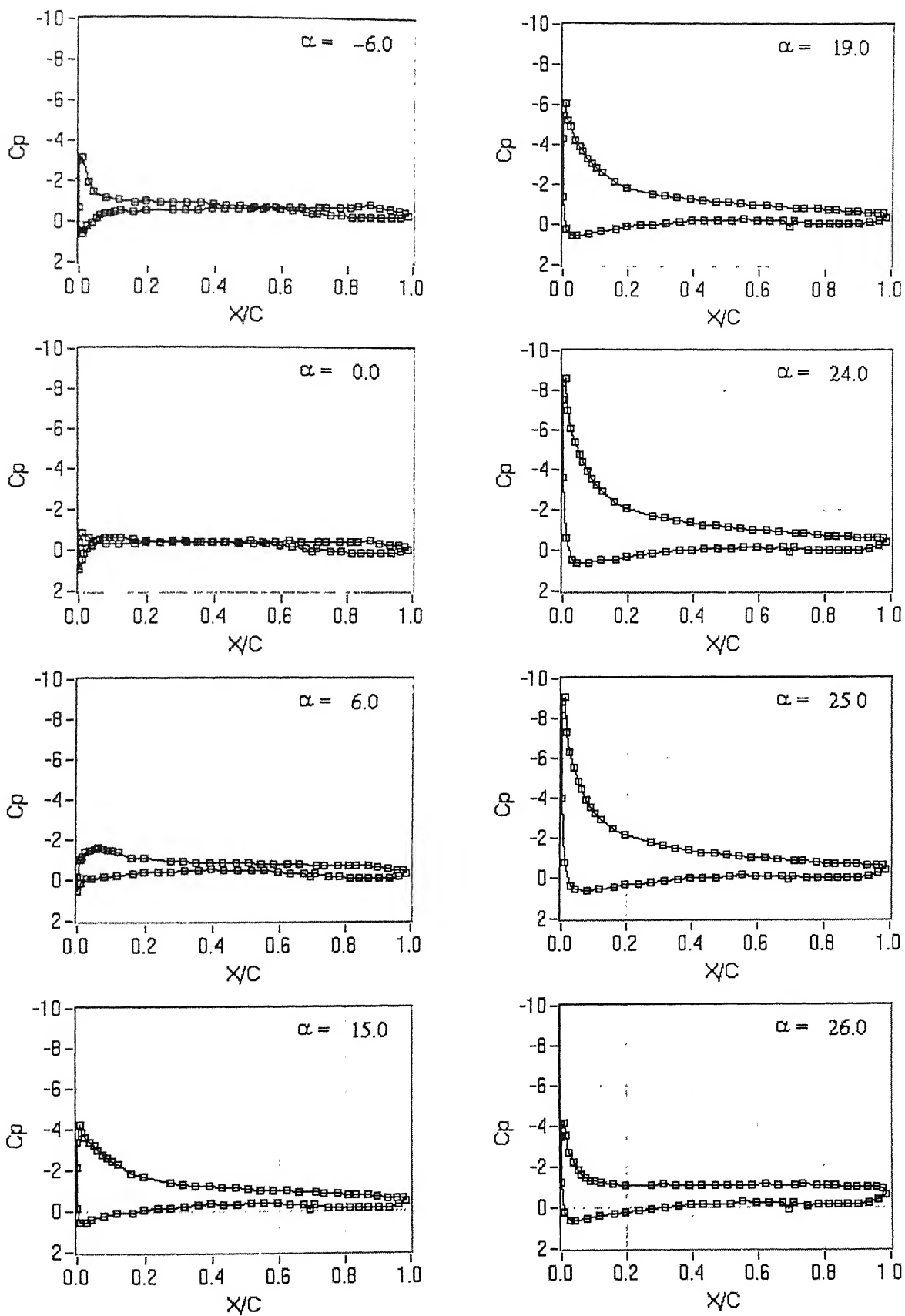
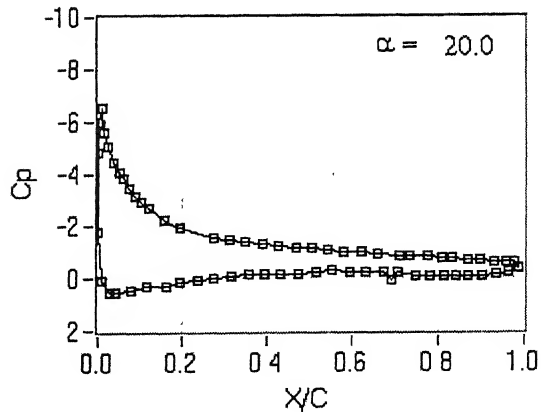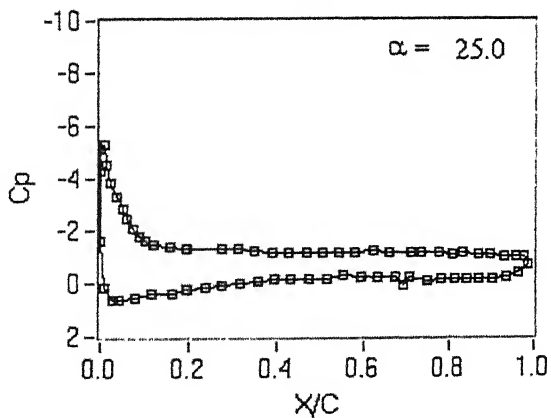Figure 7a: Surface pressure distribution on the airfoil at different angle of attack for
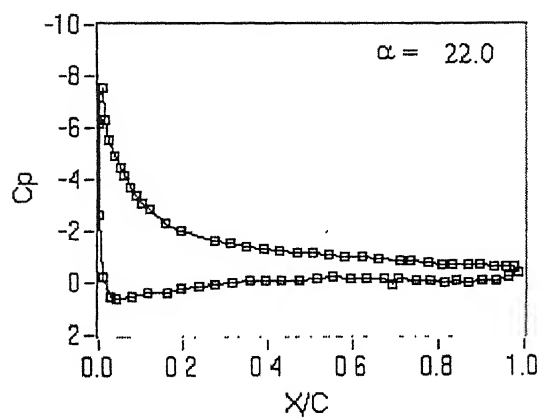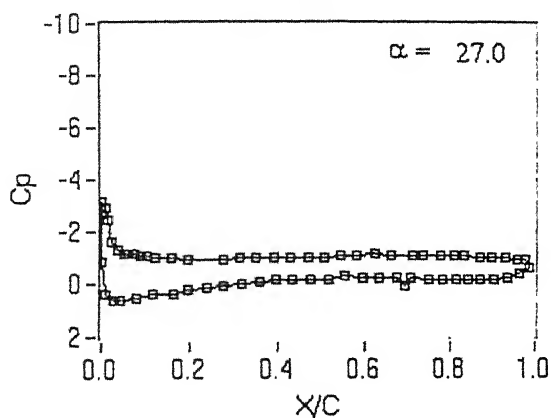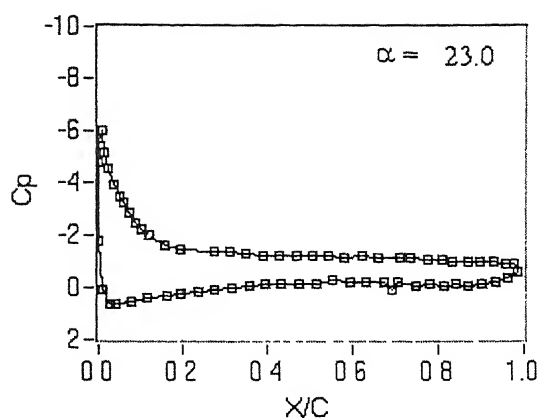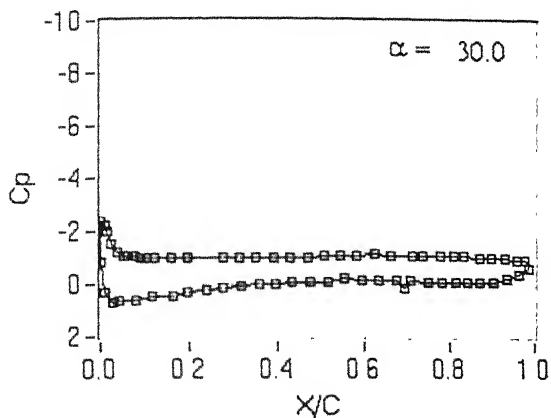retracted configuration.

Figure 7b: Surface pressure distribution on the airfoil at different angle of attack for retracted configuration.
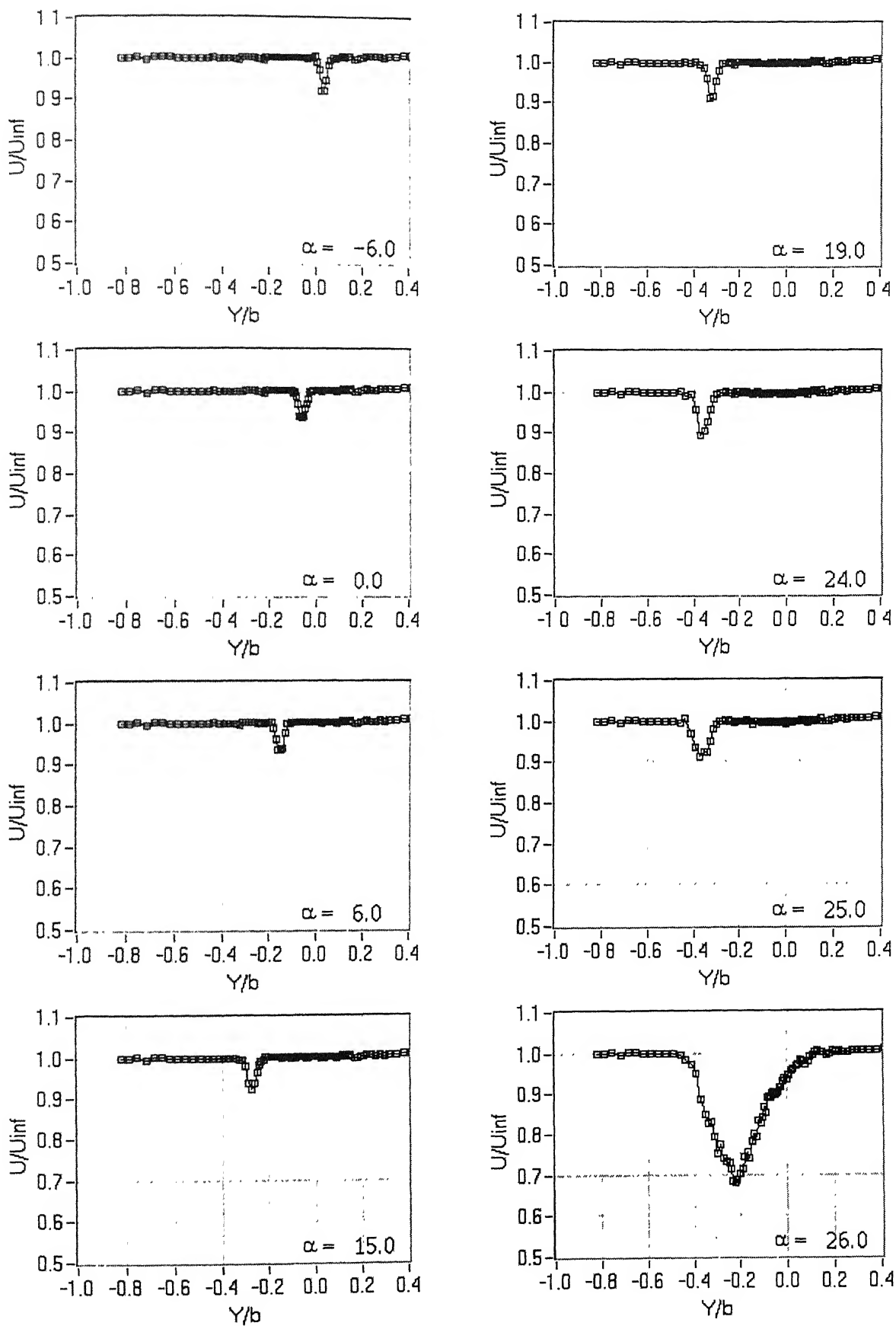
Figure 8a: Airfoil wake profiles at different angle of attack for retracted configuration.
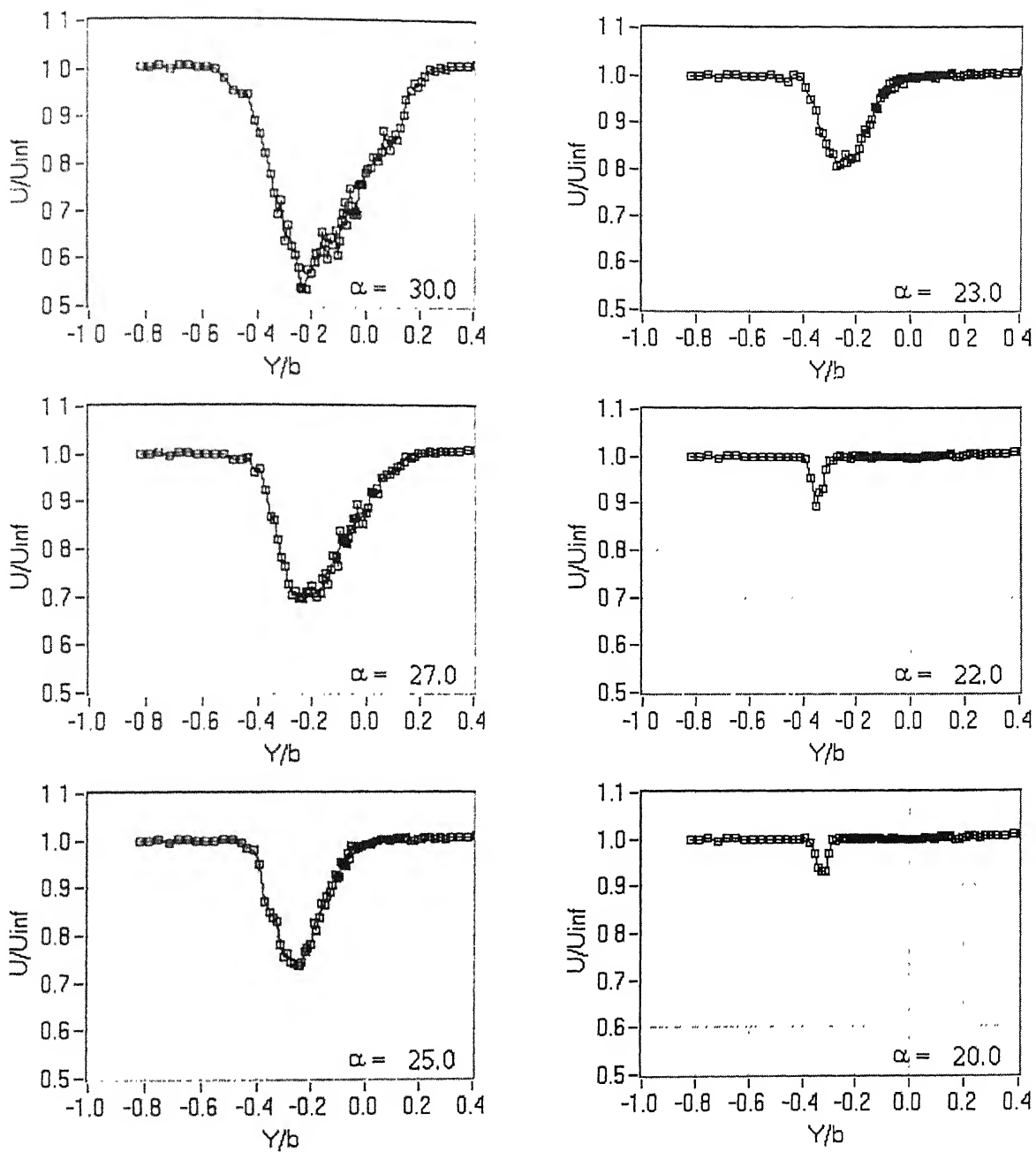
Figure 8b: Airfoil wake profiles at different angle of attack for retracted configuration.
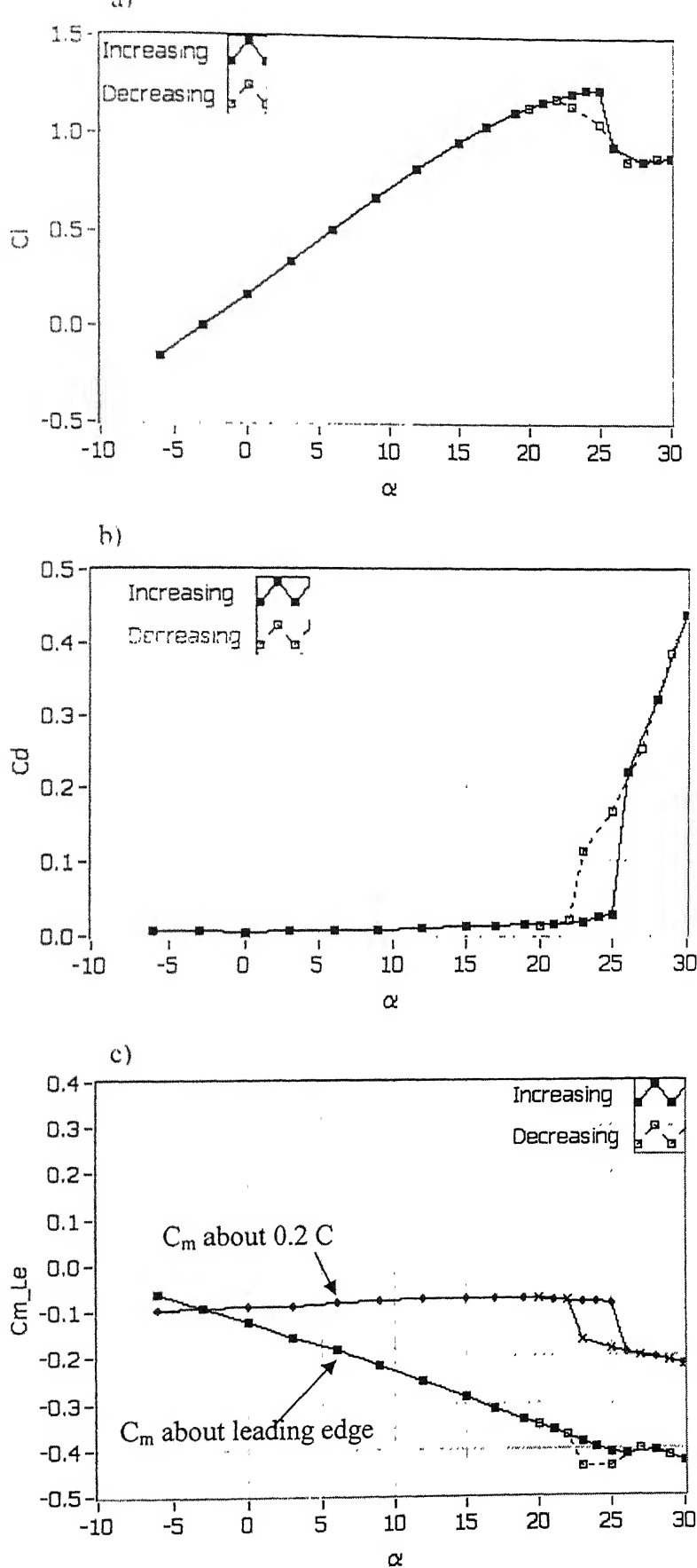
Figure 9: Variation of sectional properties of the airfoil with angle of attack
for retracted configuration: a) Lift coefficient, b) Drag coefficient,
and c) Pitching moment coefficient about leading edge.
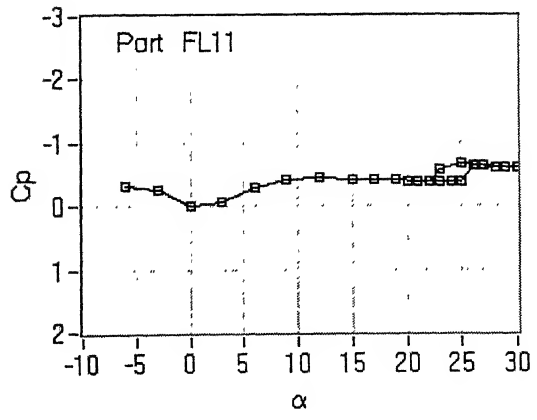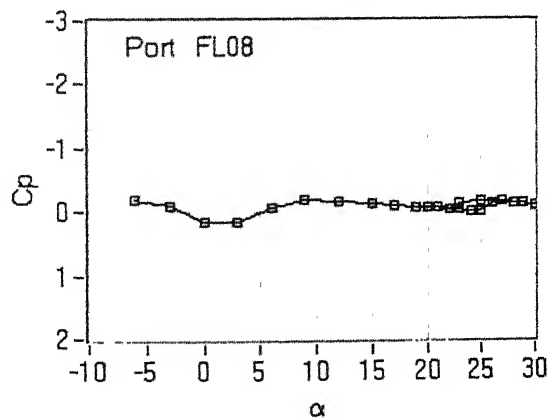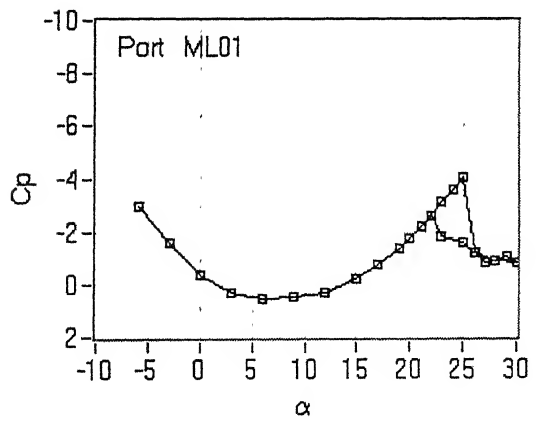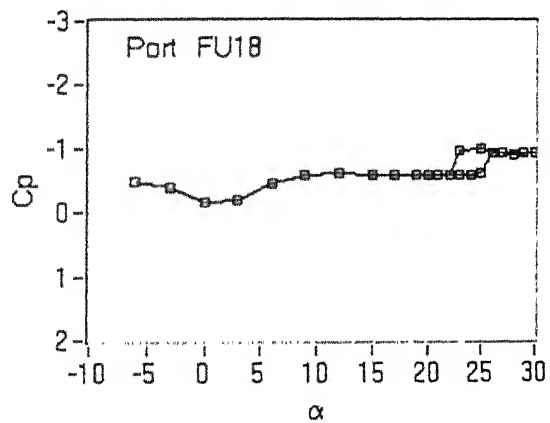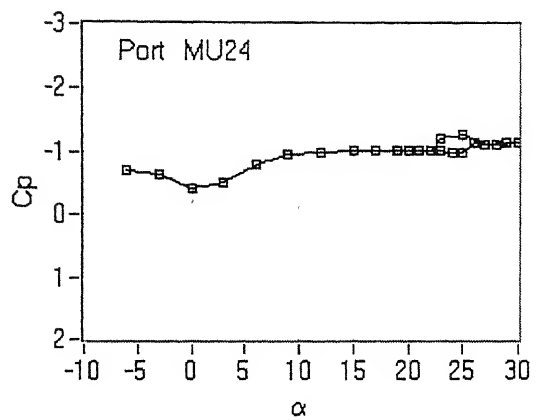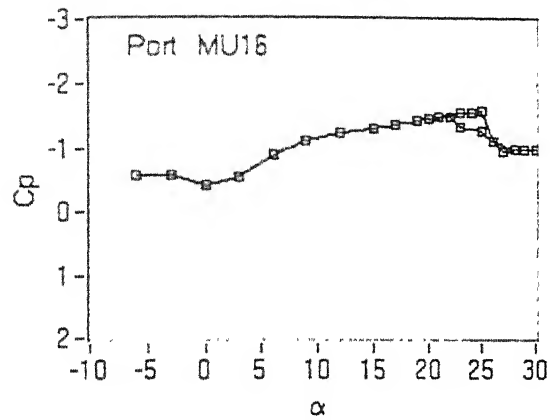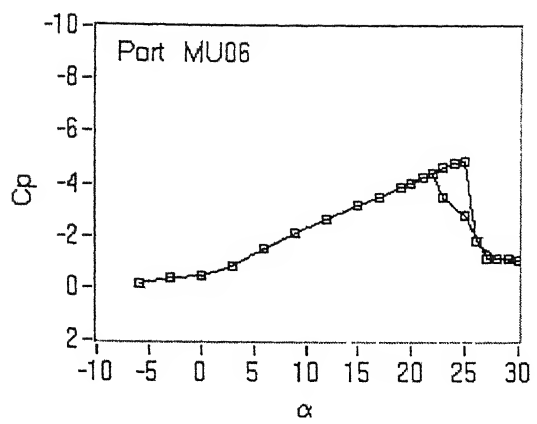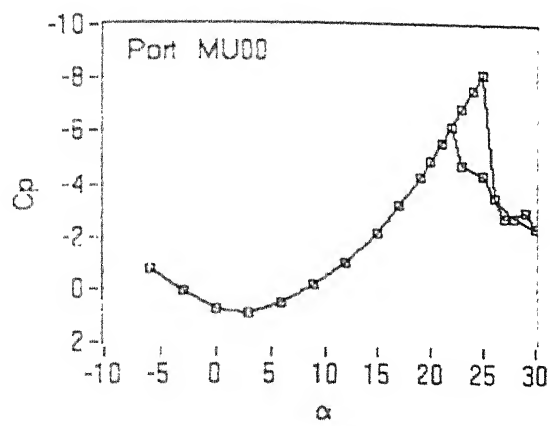
Figure10: Variation of surface pressure with angle of attack at different ports on
the airfoil for retracted configuration.
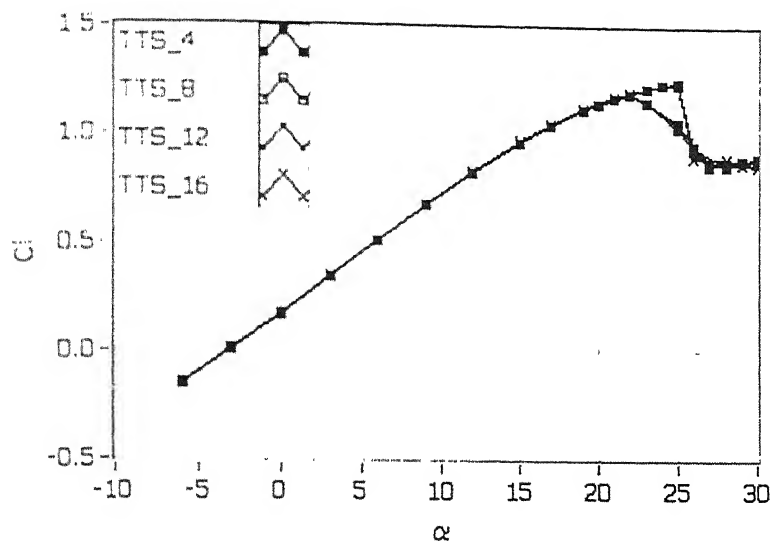
Figure 11a: Variation of lift coefficient with angle of attack at different turntable speeds.
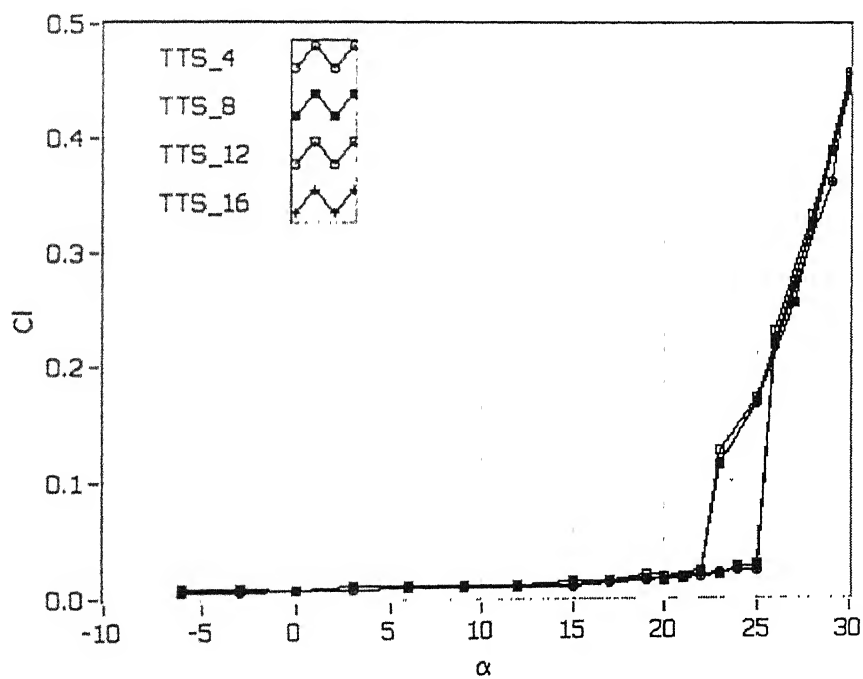
Figure 11b: Variation of drag coefficient with angle of attack at different turntable speeds.
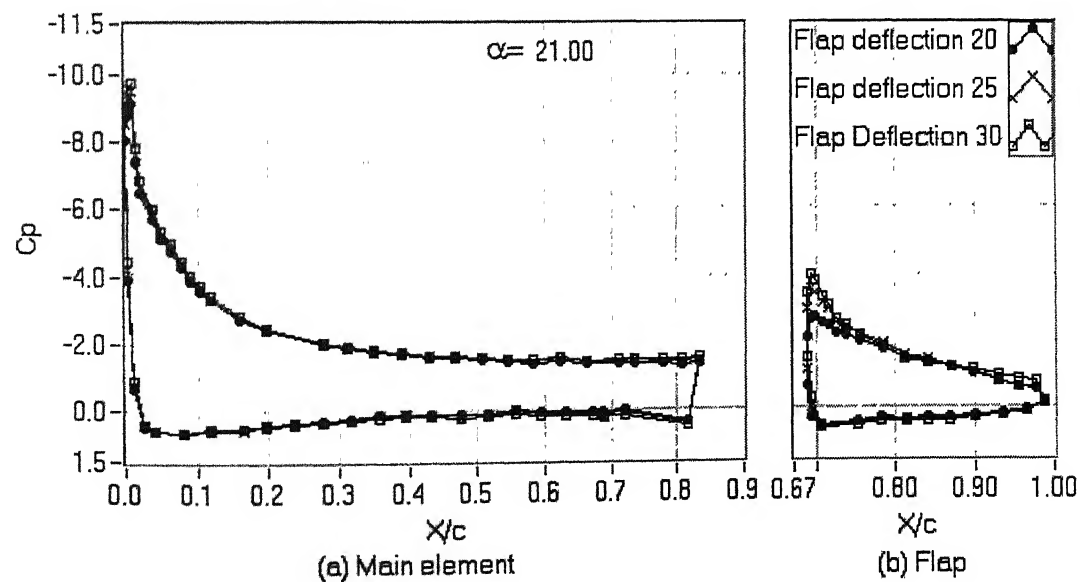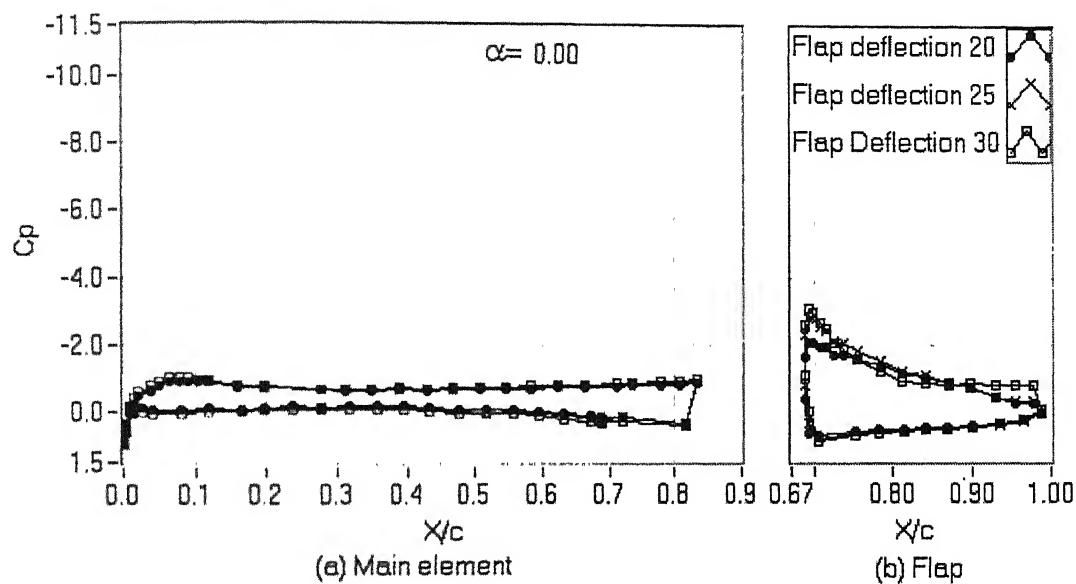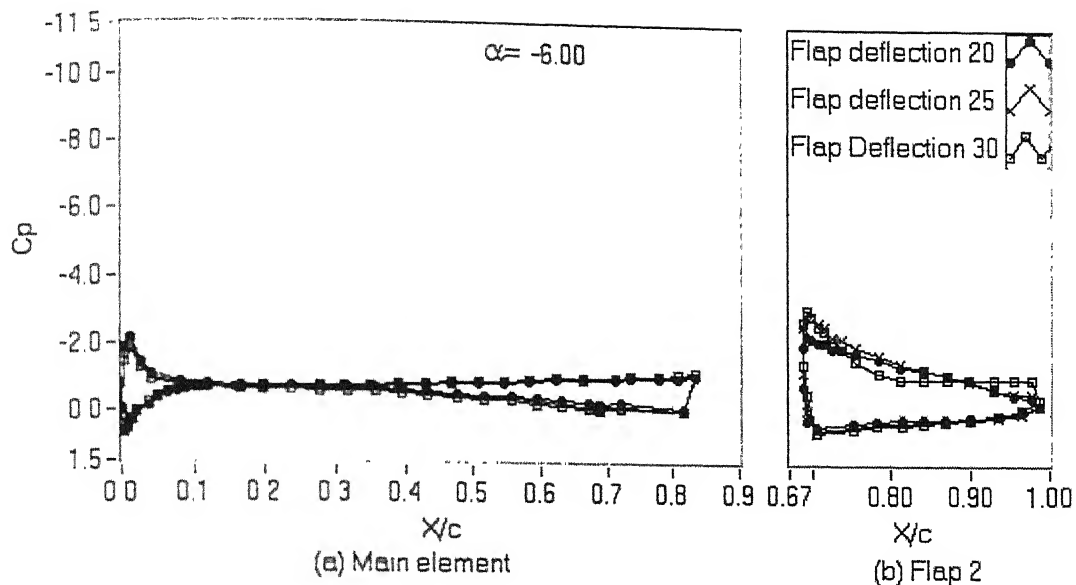
Figure 12a: Surface pressure distribution on the two-element airfoil at 0% overhang
for α= -6⁰, 0⁰, and 21⁰.
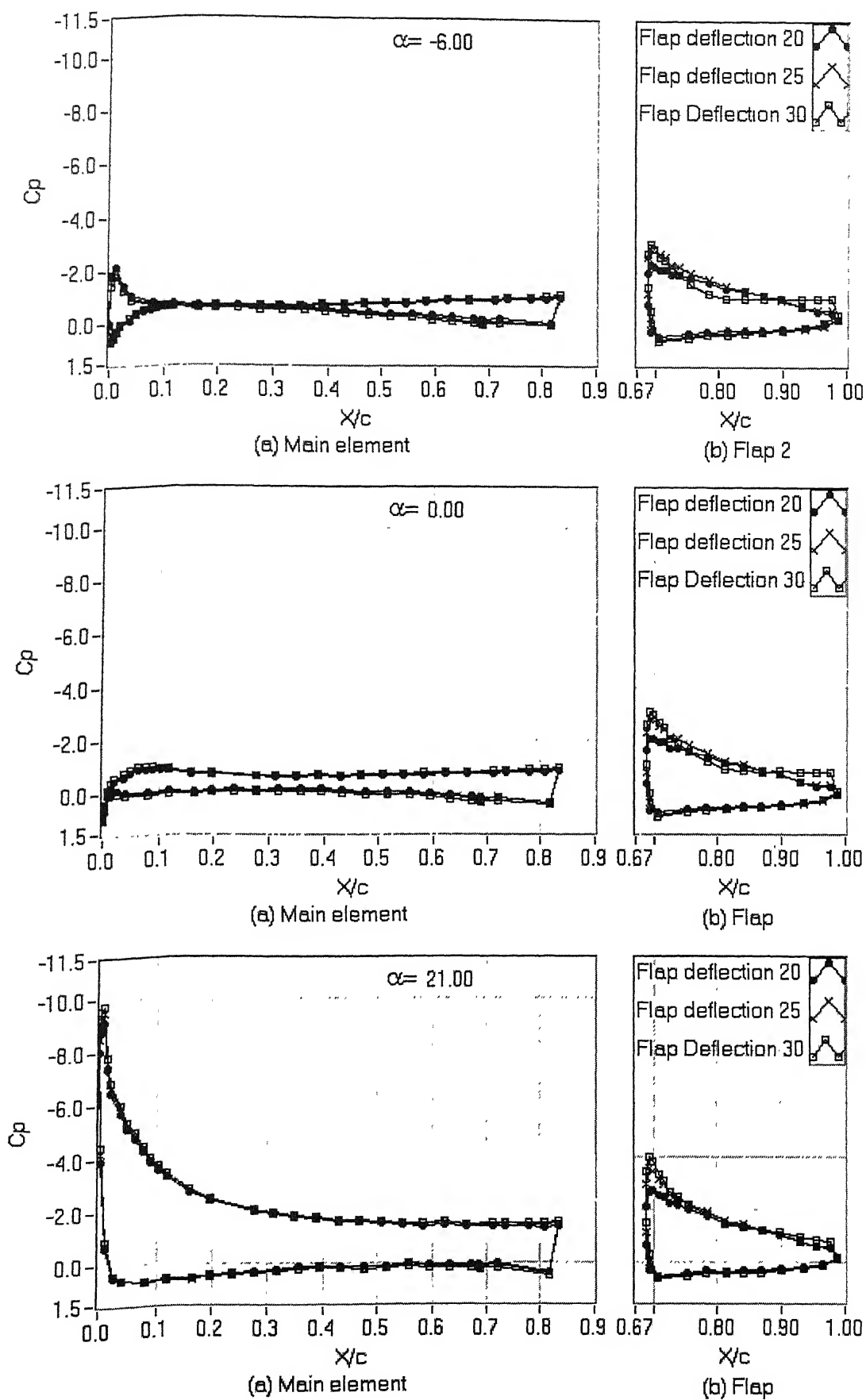
Figure 12a: Surface pressure distribution on the two-element airfoil at 0% overhang for α= -6^0, 0^0, and 21^0.
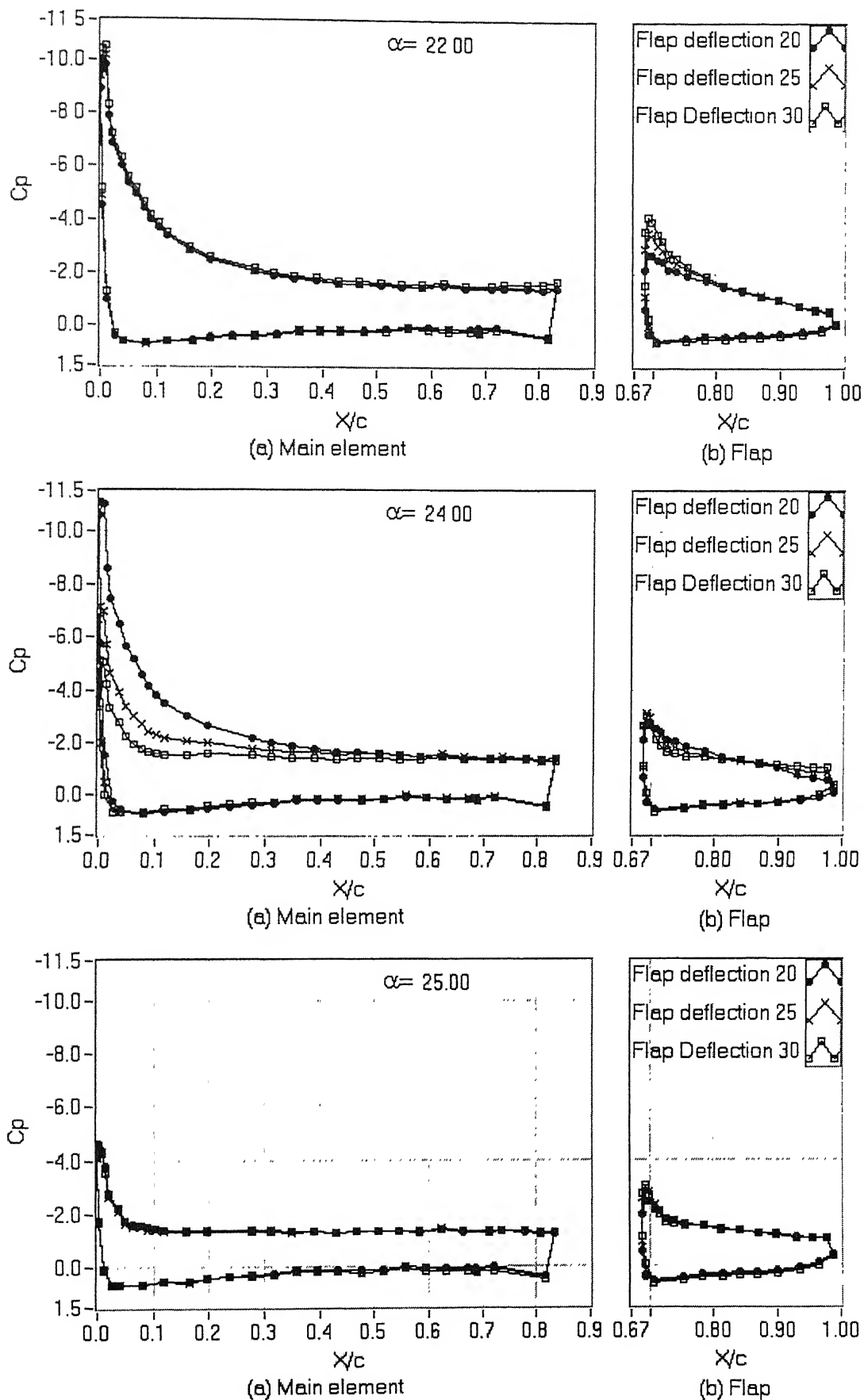
Figure 12b: Surface pressure distribution on the two-element airfoil at 0% overhang for $\alpha = 22^0$, 24^0, and 25^0.
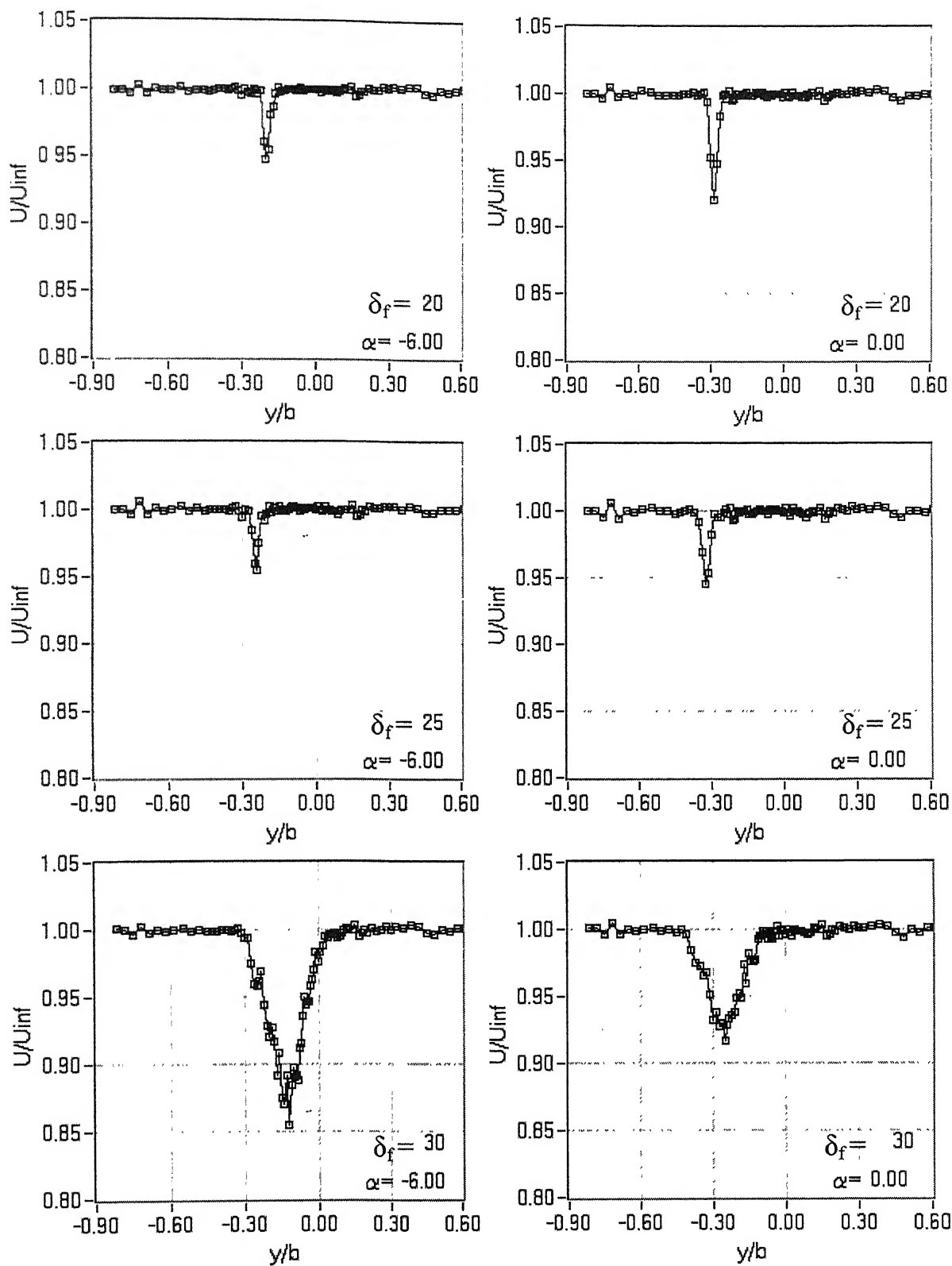
Figure 13a: Wake profiles for two-element airfoil at 0% overhang for $\alpha = -6^0$ and 0^0.
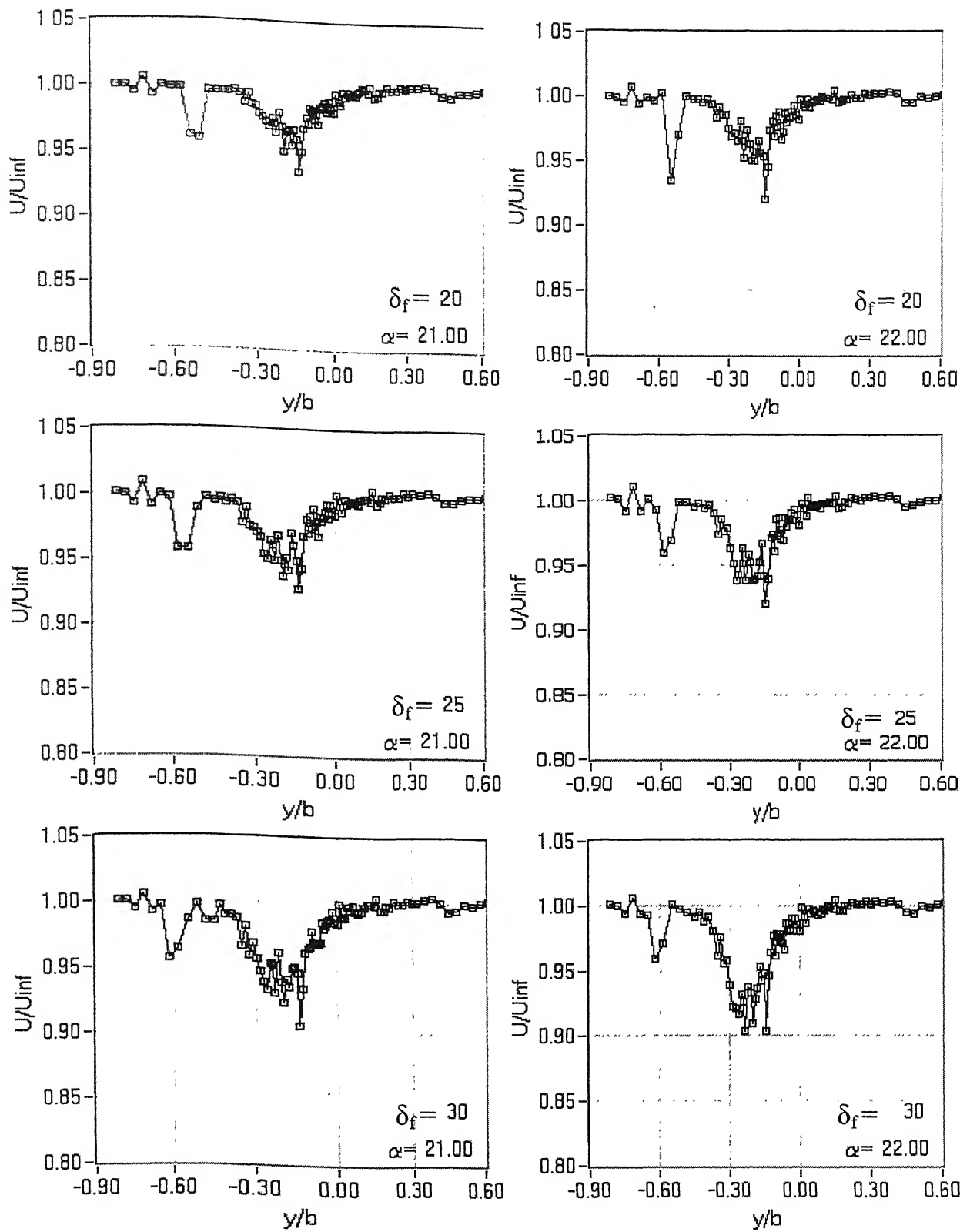
Figure 13b: Wake profile for two-element airfoil at 0% overhang for $\alpha = 21^0$ and 22^0.
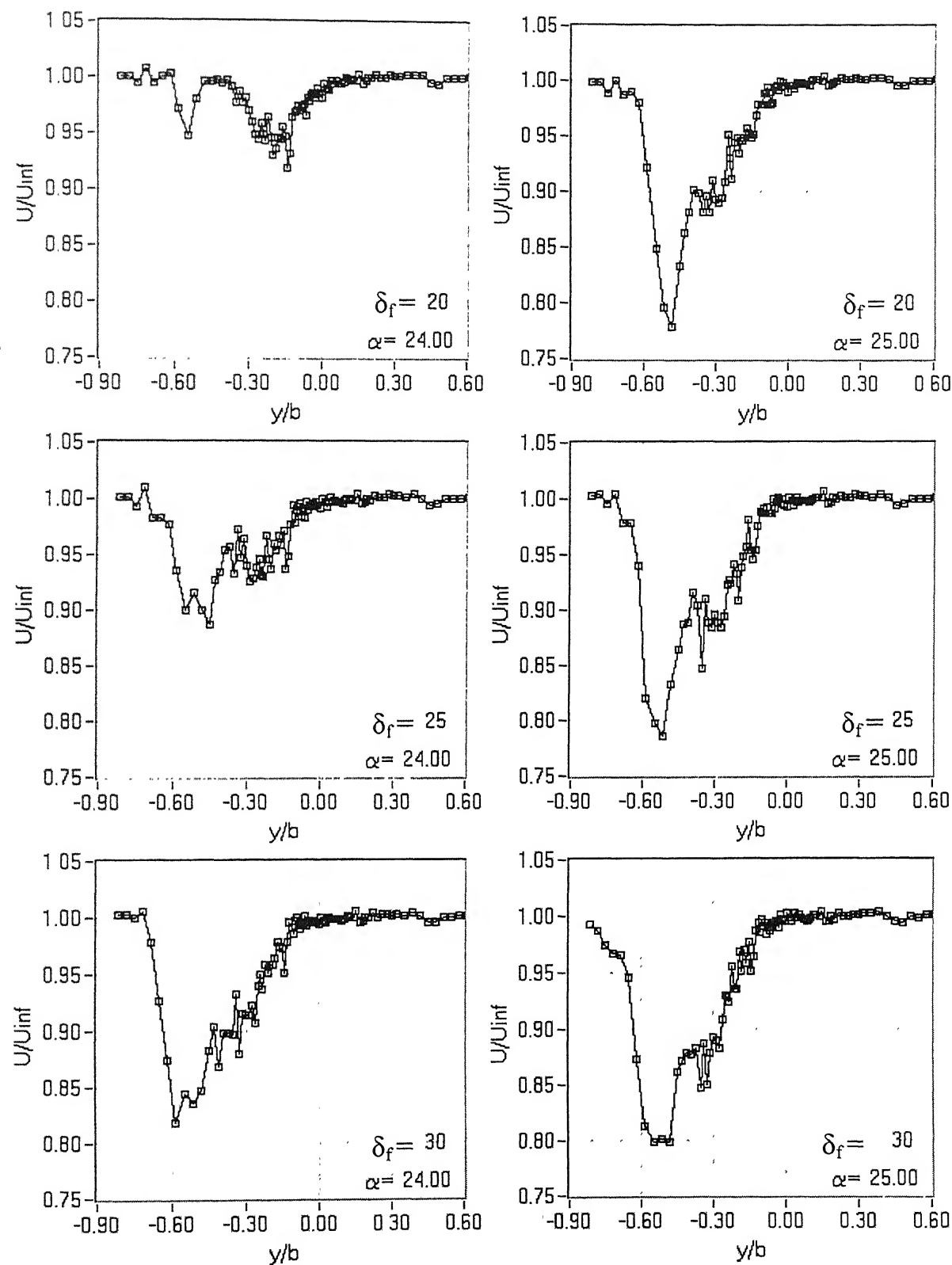
Figure 13c: Wake profile for two-element airfoil at 0% overhang for $\alpha = 24^0$ and 25^0.
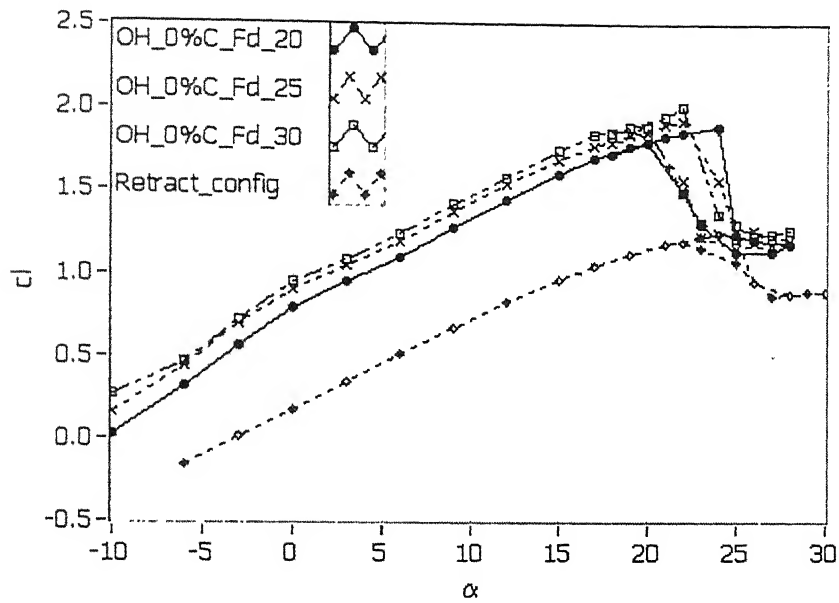
Figure 14a: Variation of lift coefficient with angle of attack at 0% overhang for 20^0, 25^0, and 30^0 flap deflections.
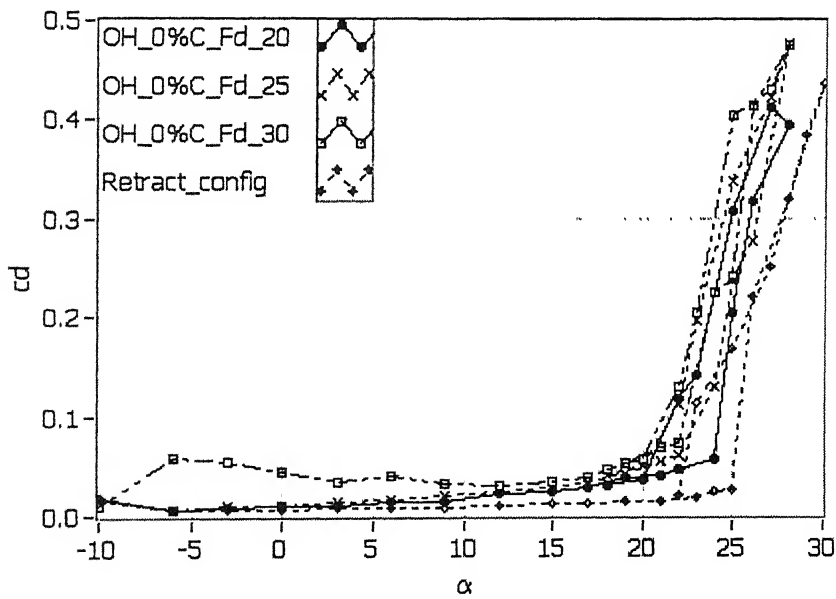
Figure 14b: Variation of lift coefficient with angle of attack at 0% overhang for 20^0, 25^0, and 30^0 flap deflections.
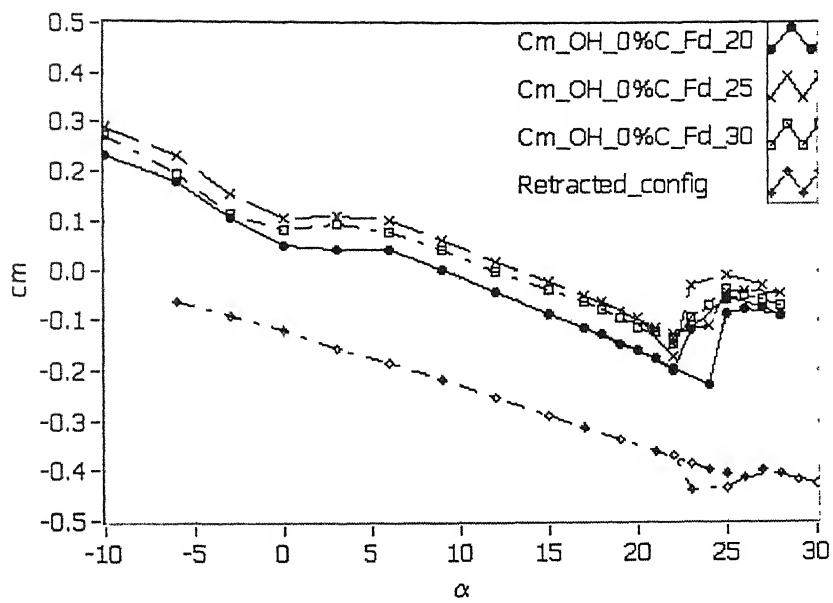
Figure 14c: Variation of pitching moment coefficient with angle of attack at 0% overhang for 20^0, 25^0, and 30^0 flap deflections.
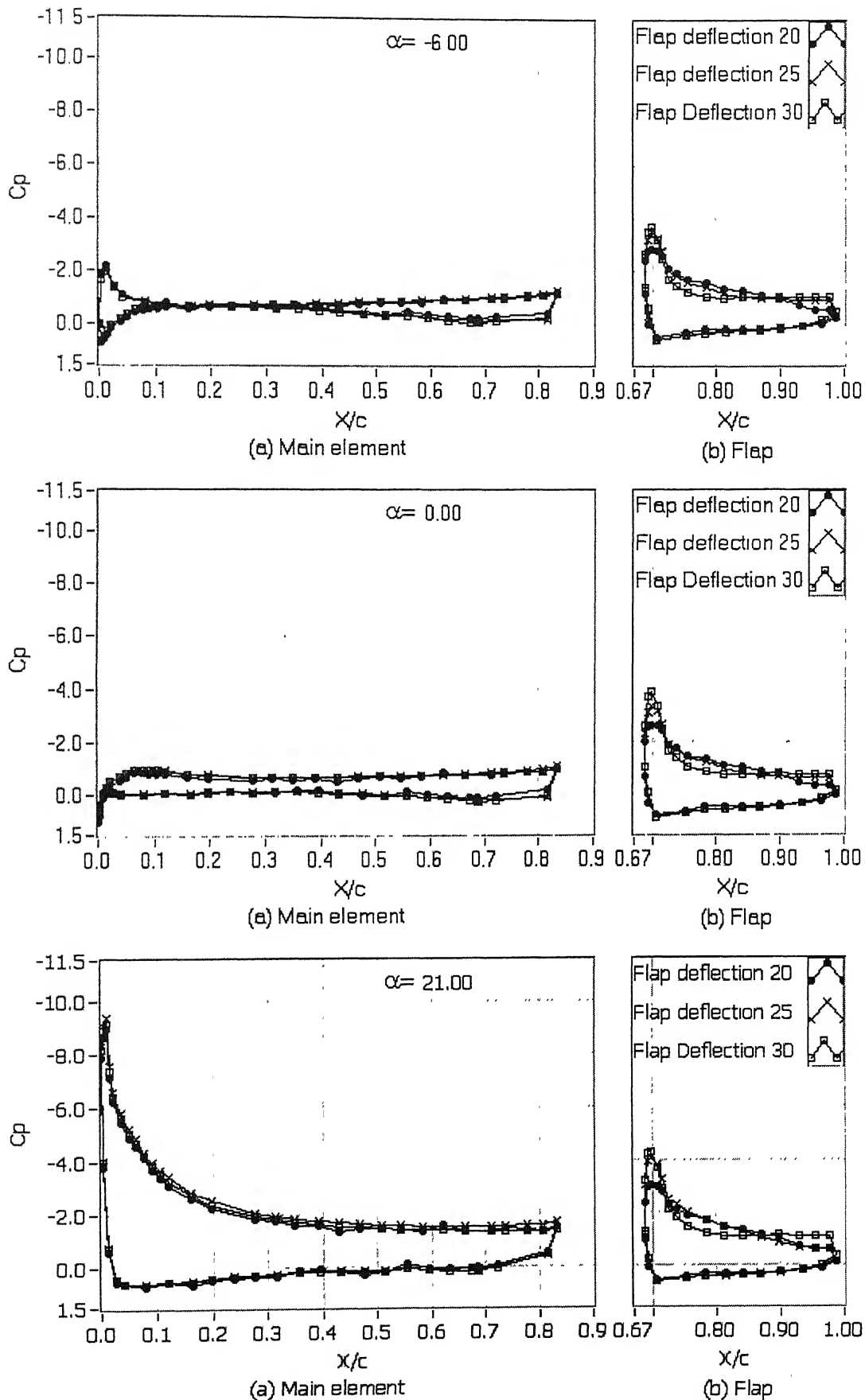
Figure 15a: Surface pressure distribution on the two-element airfoil at 5.23% overhang for $\alpha = -6^0, 0^0,$ and 21^0.
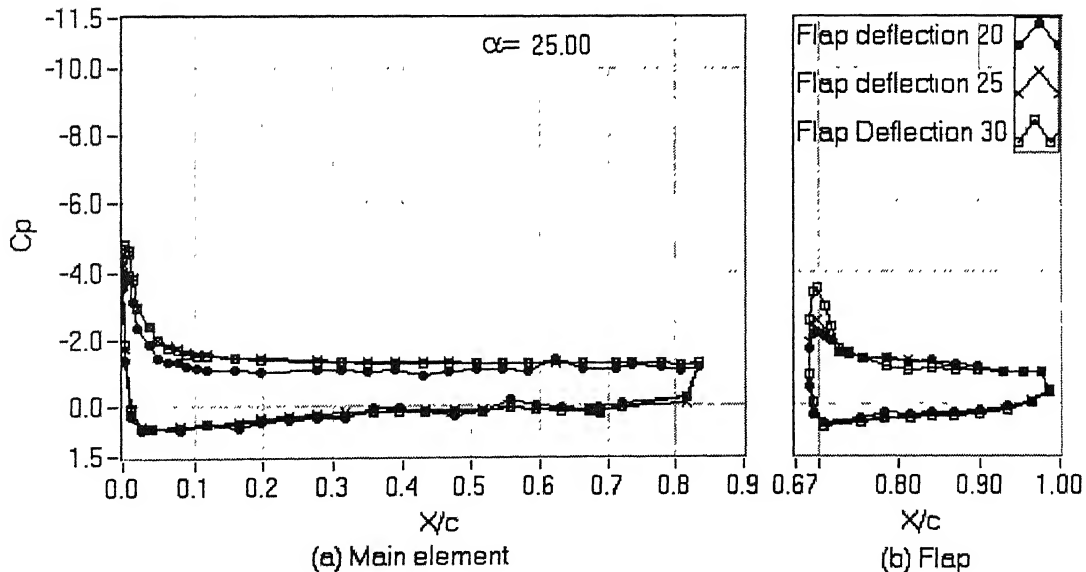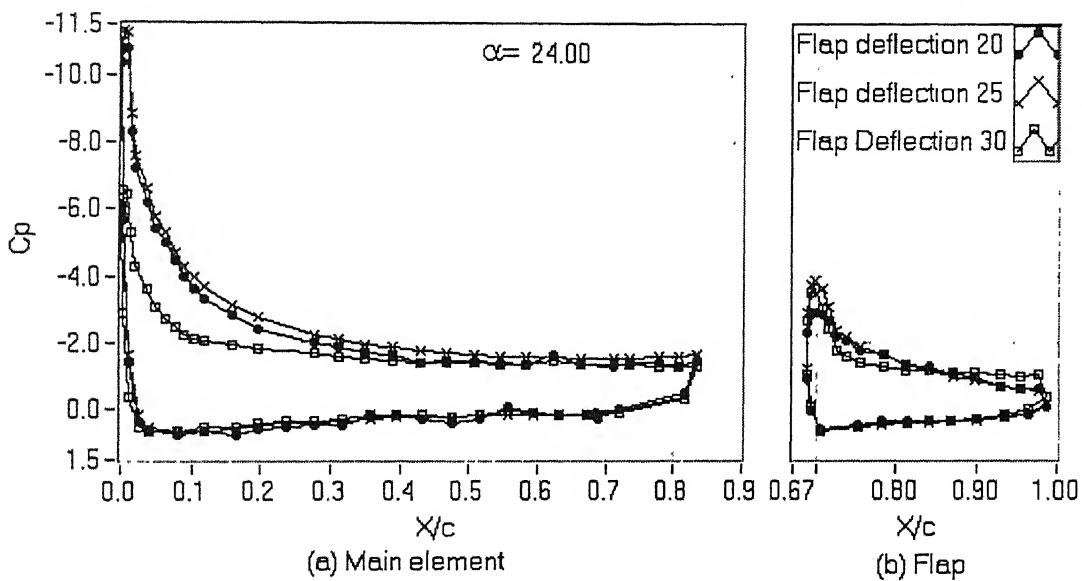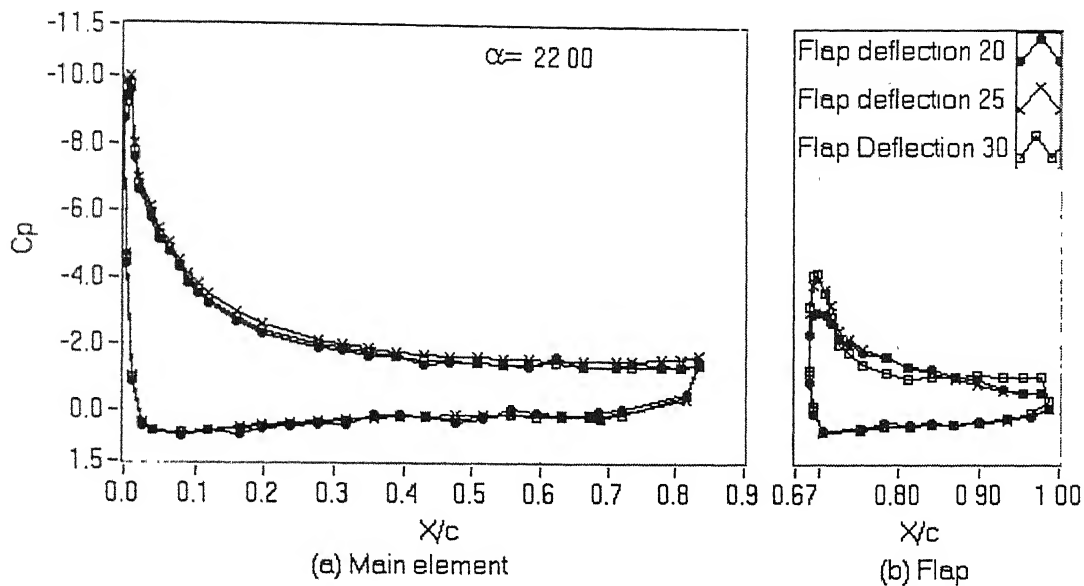
Figure 15b: Surface pressure distribution on the two-element airfoil at 5.23% overhang for $\alpha = 22^0$, 24^0, and 25^0.
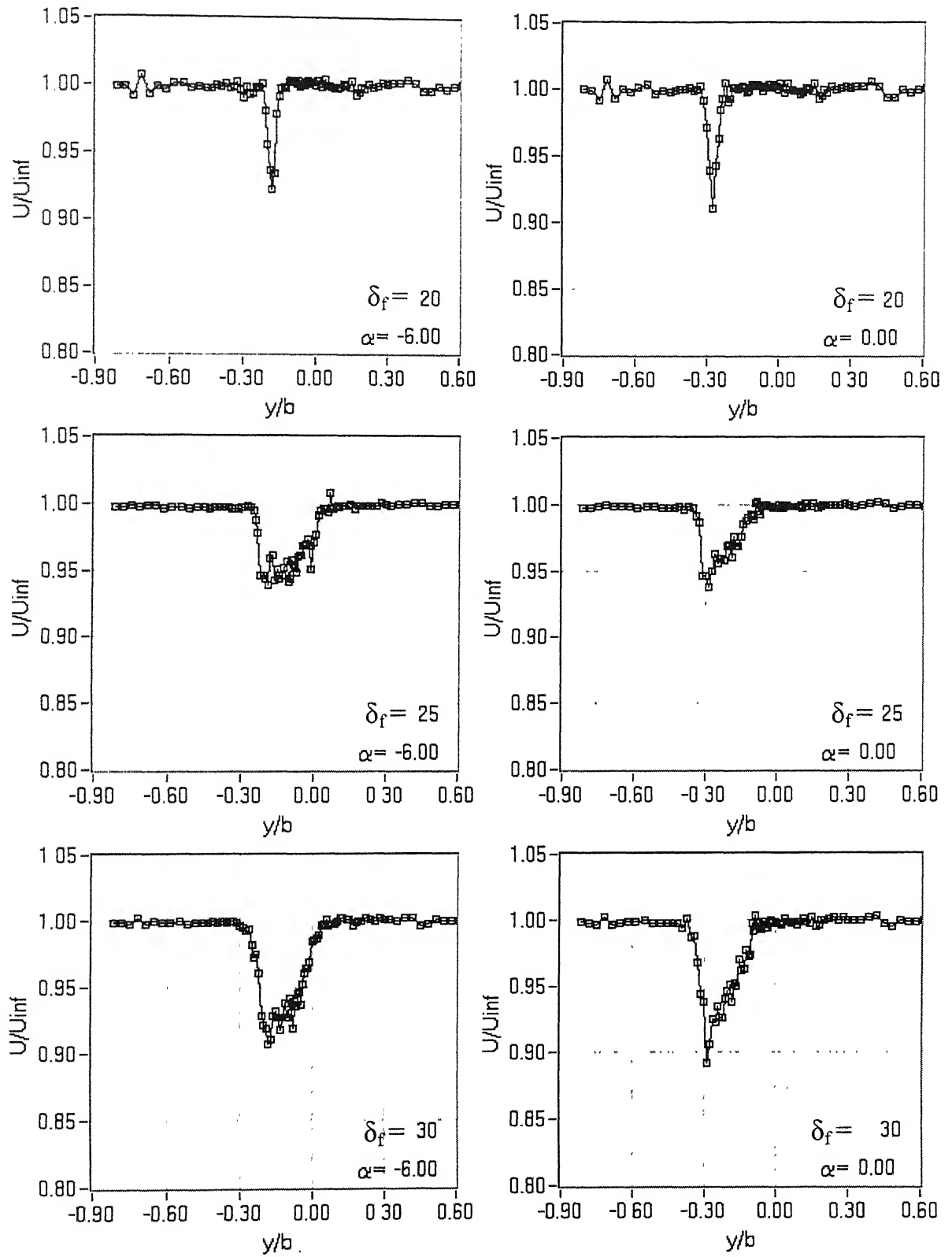
Figure 16a: Wake profiles for two-element airfoil at 5.23% overhang for $\alpha = -6^0$ and 0^0.
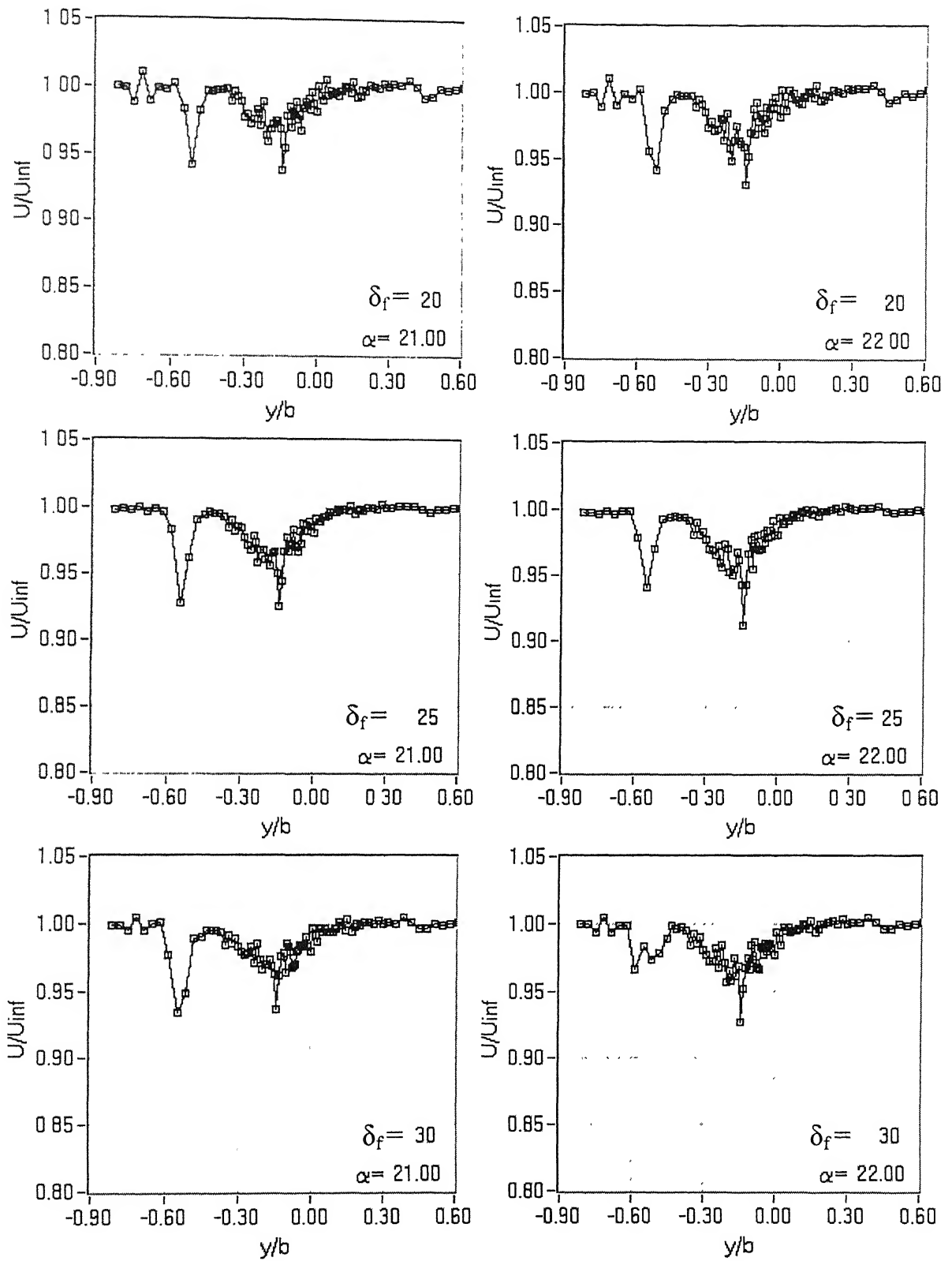
Figure 16b: Wake profiles for two-element airfoil at 5.23% overhang for $\alpha = 21^0$ and 22^0.
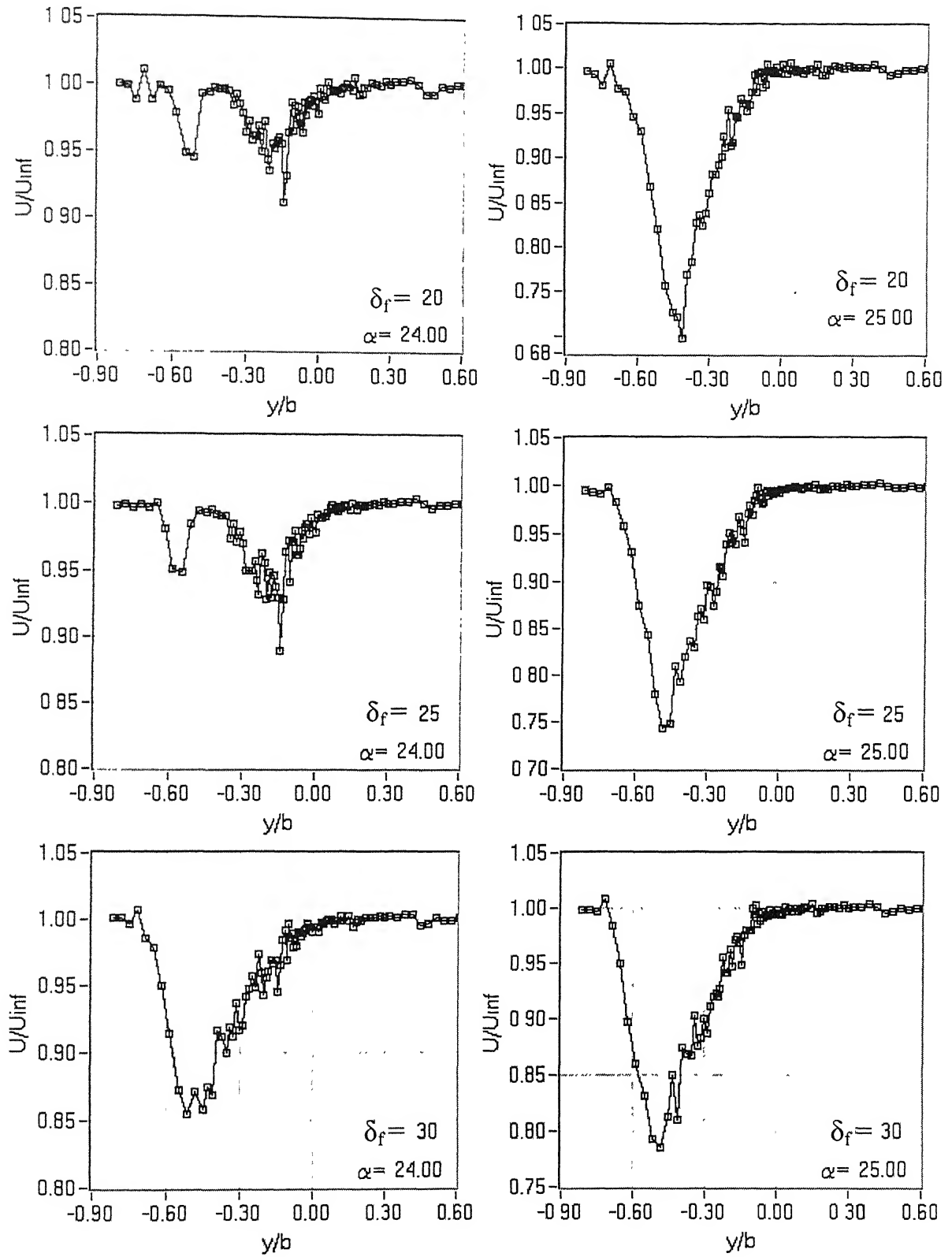
Figure 16c: Wake profiles for two-element airfoil at 5.23% overhang for $\alpha = 24^0$ and 25^0.
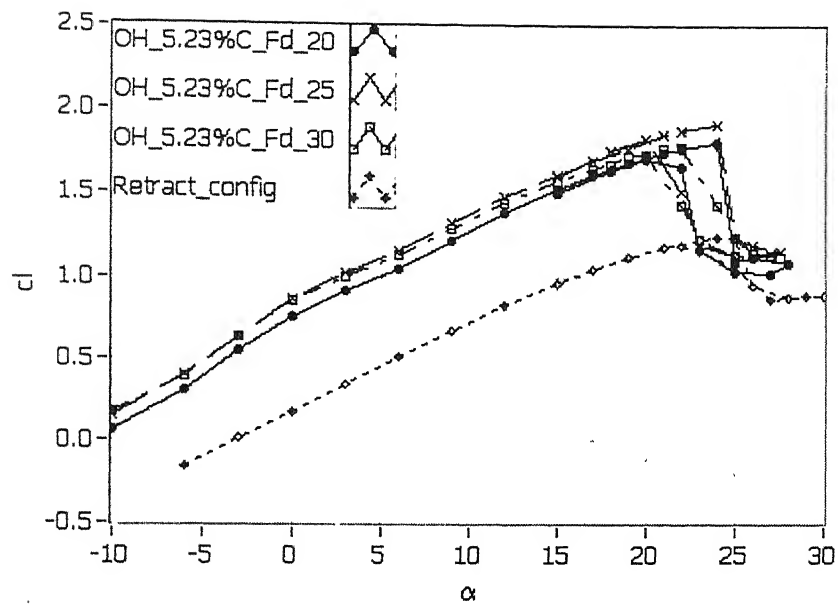
Figure 17a: Variation of lift coefficient with angle of attack at 5.23% overhang for 20^0, 25^0, and 30^0 flap deflections.
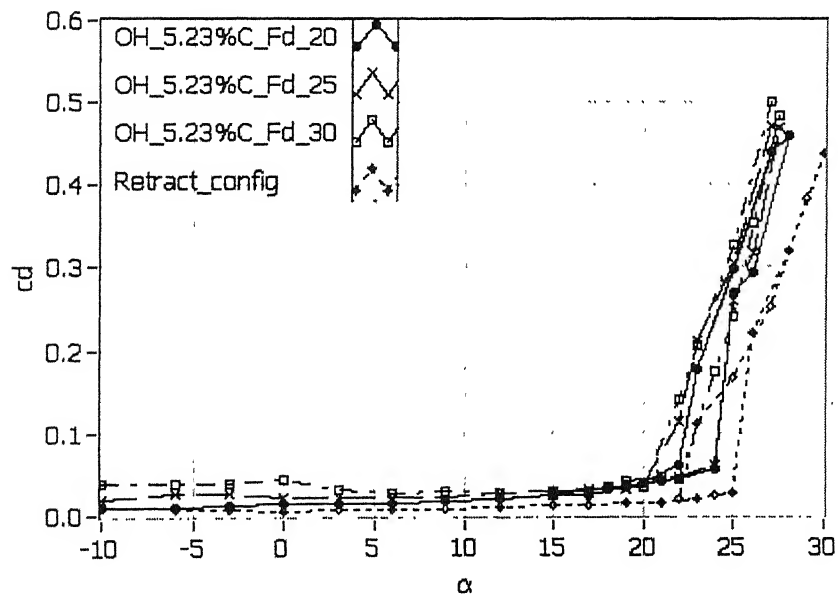
Figure 17b: Variation of drag coefficient with angle of attack at 5.23% overhang for 20^0, 25^0, and 30^0 flap deflections.
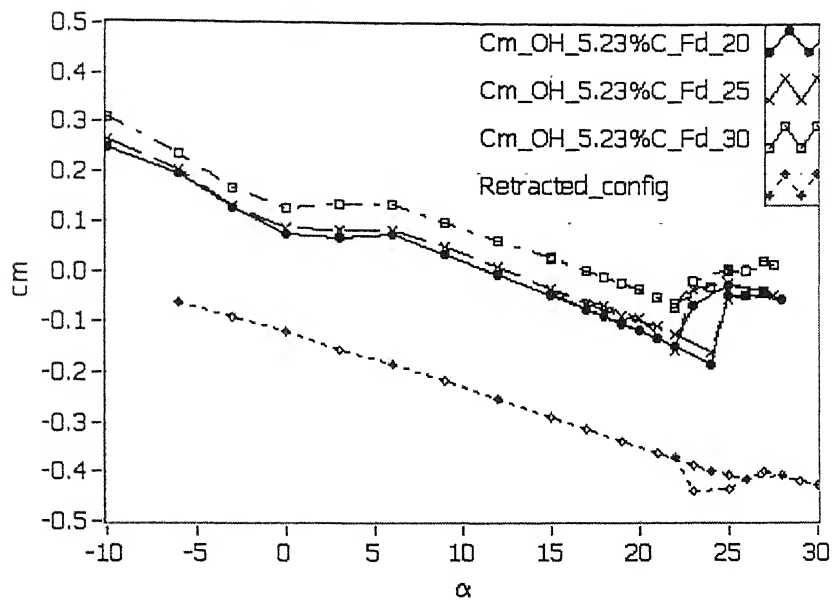
Figure 17c: Variation of pitching moment coefficient with angle of attack at 5.23% overhang for 20^0, 25^0, and 30^0 flap deflections.
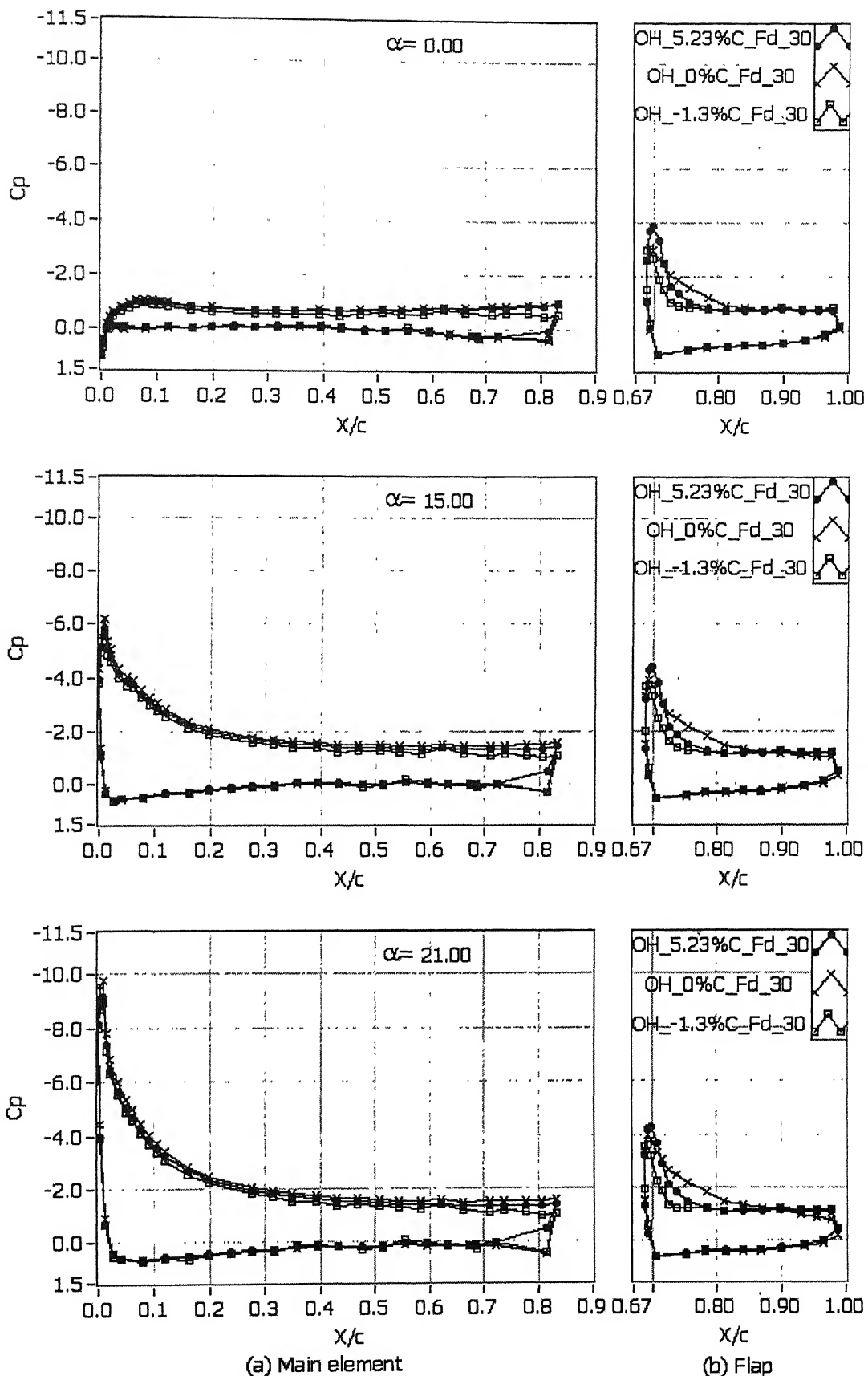
Figure 18a: Surface pressure distribution on the two-element airfoil for $\alpha = 0^0$, 15^0, and 21^0 at 0%, 5.23%, -1.3% overhangs and 30^0 flap deflection.
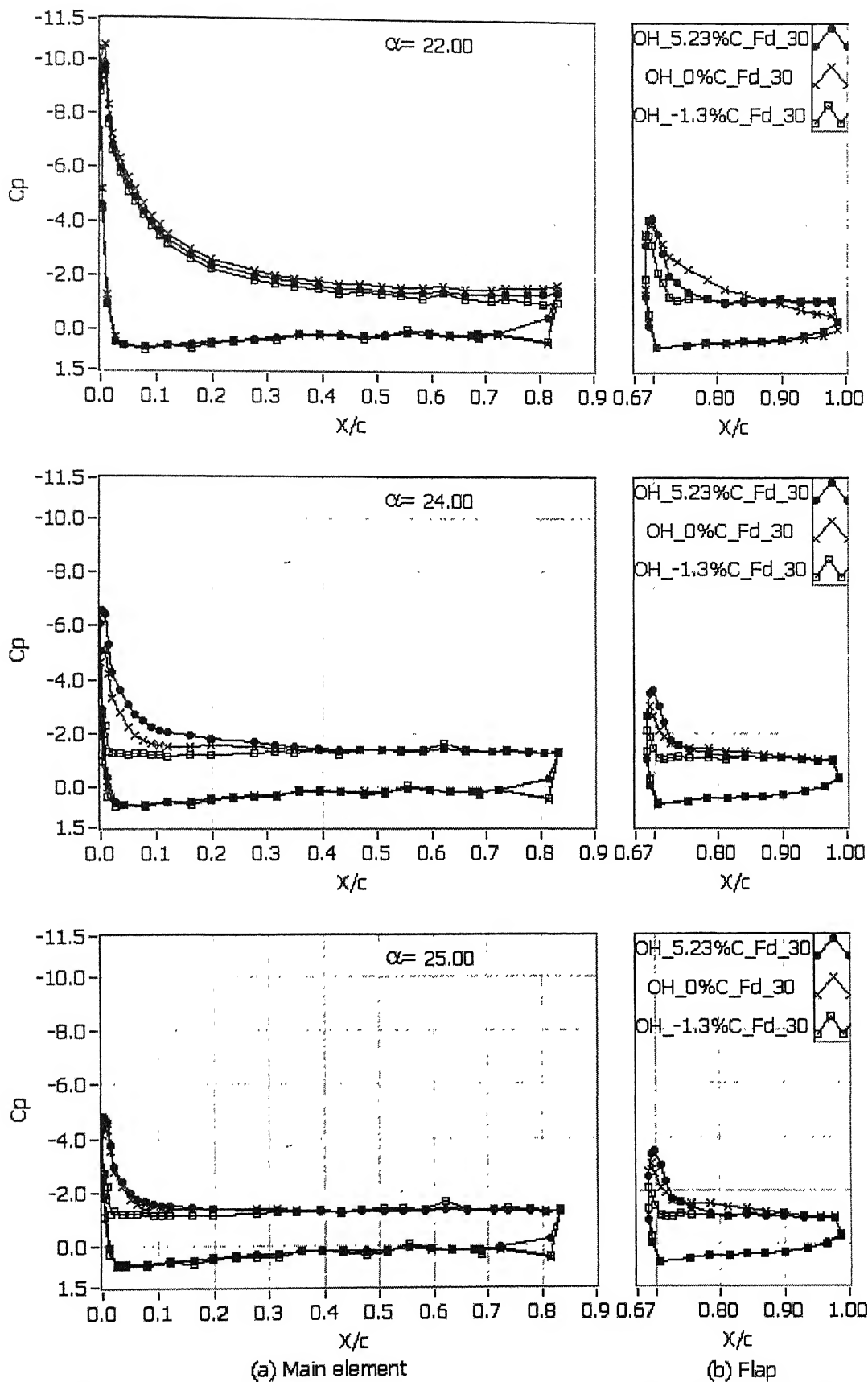
Figure 18b: Surface pressure distribution on the two-element airfoil for $\alpha=22^0$, 24^0 and 25^0 at 0%, 5.23% and, -1.3% overhangs and 30^0 flap deflection.
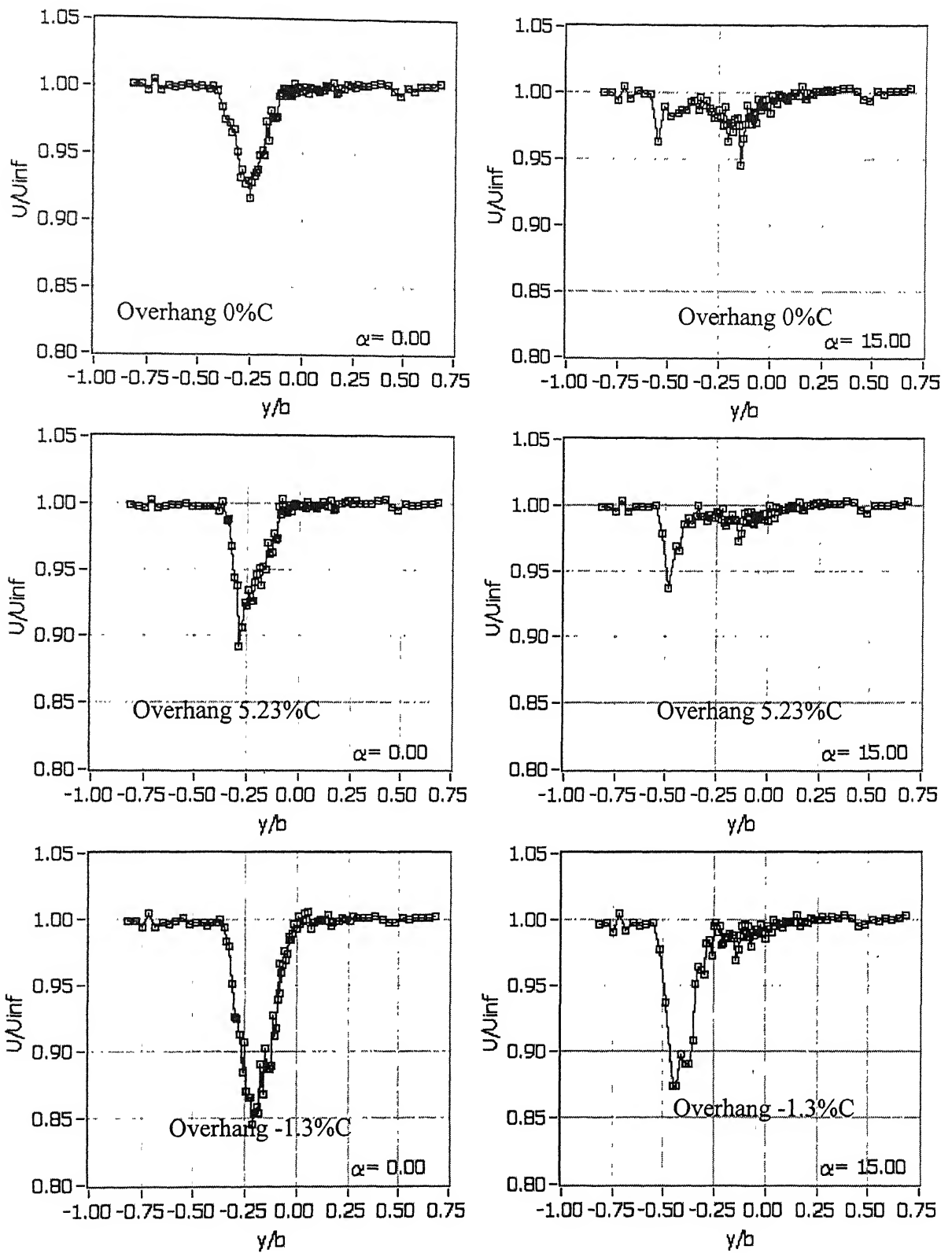
Figure 19a: Wake profile for two-element airfoil for $\alpha = 0^0$ and 15^0 at 0%, 5.23%, -1.3% overhangs and 30^0 flap deflection.
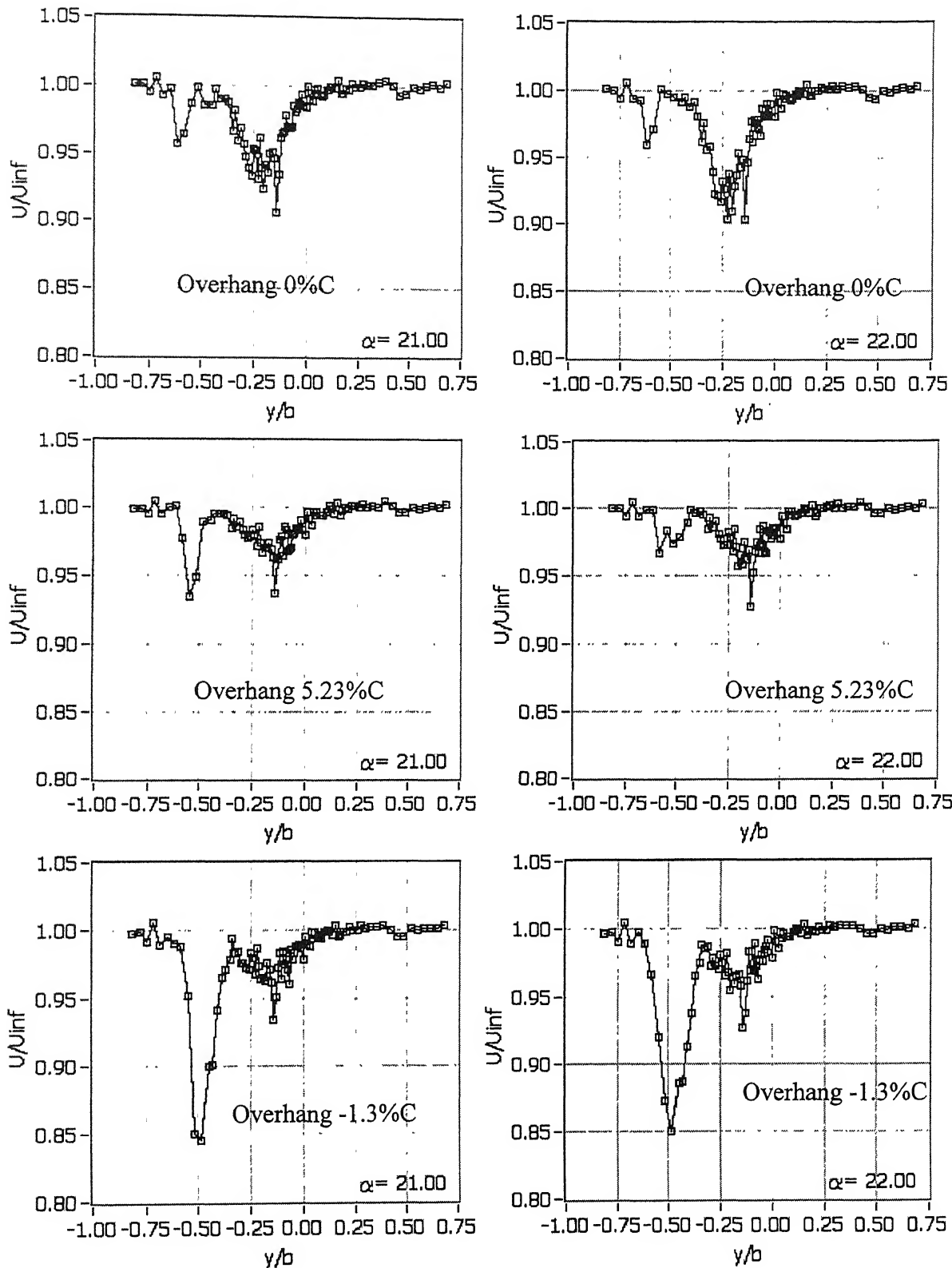
Figure 19b: Wake profile for two-element airfoil for $\alpha = 21^0$ and 22^0 at 0%, 5.23%, -1.3% overhangs and 30^0 flap deflection.
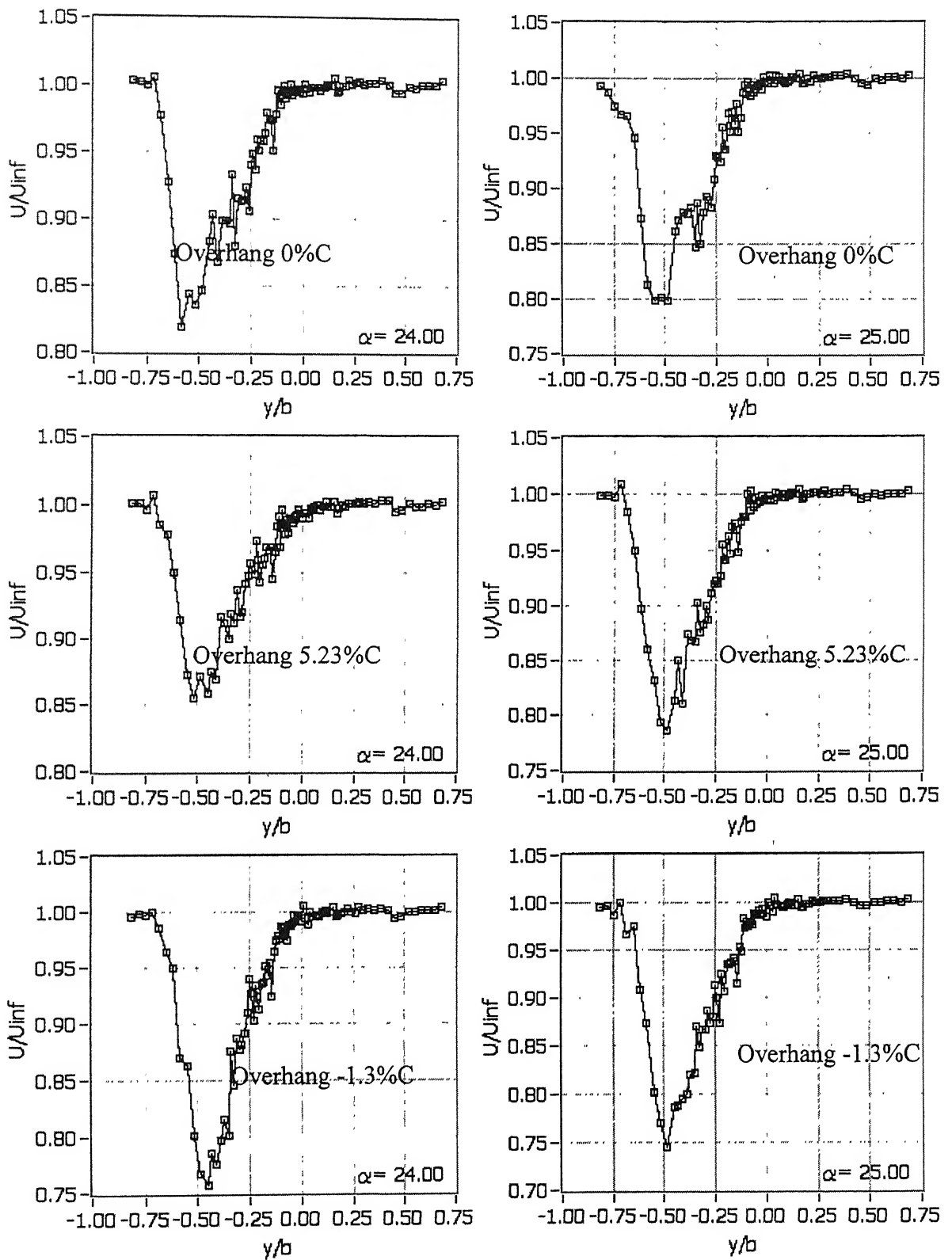
Figure 19c: Wake profile for two-element airfoil for $\alpha = 24^0$ and 25^0 at 0%, 5.23%, -1.3% overhangs and 30^0 flap deflection.
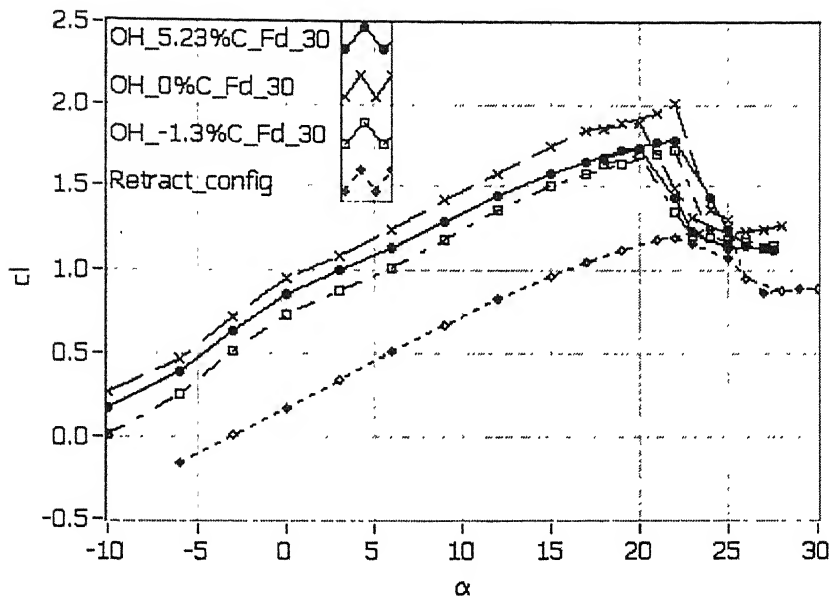
Figure 20a: Variation of lift coefficient with angle of attack for 0%, 5.23%, and -1.3% overhangs and 30^0 flap deflections.
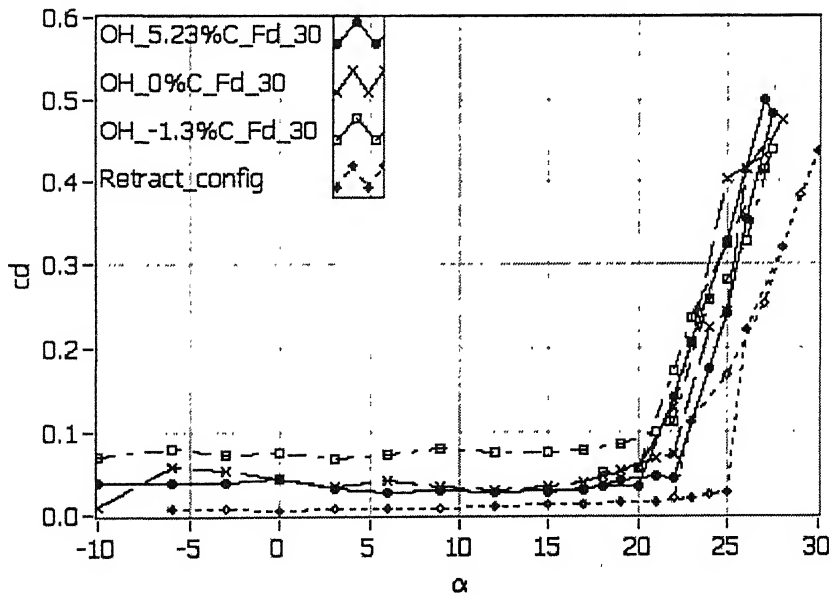
Figure 20b: Variation of lift coefficient with angle of attack for 0%,5.23%, and -1.3% overhangs and 30^0 flap deflections.
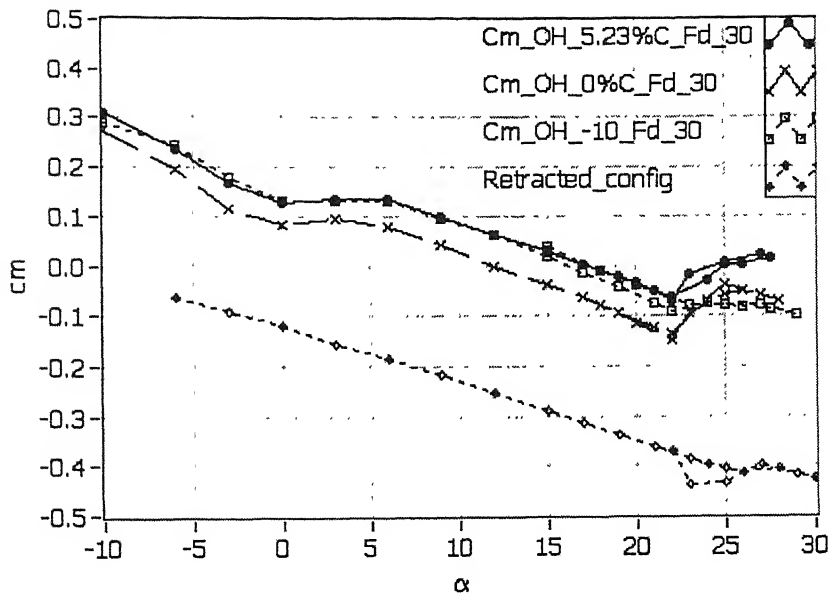
Figure 20c: Variation of pitching moment coefficient with angle of attack for 0%, 5.23%, and -1.3% overhangs and 30^0 flap deflection.

Table 1a: Two-element airfoil coordinates for main element

	Upper surface			Lower surface	
S. No	X	Y	S. No	X	Y
1	0.8	4.493	1	0.000	-1.295
2	2.15	7.892	2	0.800	-5.005
3	4.15	11.302	3	4.150	-9.851
4	7.35	15.329	4	11.350	-12.917
5	11.35	19.242	5	20.950	-14.765
6	16.15	23.067	6	36.950	-17.429
7	20.95	26.311	7	88.950	-23.874
8	26.95	29.811	8	144.950	-28.344
9	33.35	33.056	9	204.950	-30.979
10	40.95	36.42	10	264.950	-31.486
11	50.95	40.227	11	324.950	-29.468
12	62.95	44.072	12	384.950	-24.360
13	70.95	46.278	13	444.950	-16.055
14	78.95	48.235	14	484.950	-9.119
15	86.95	49.859	15	508.950	-4.688
16	96.95	51.145	16	524.950	-1.713
17	108.95	52.331	17	524.950	17.981
18	124.95	53.764	18	524.950	37.675
19	144.95	55.339	19	564.950	37.675
20	164.95	56.703	20	584.950	37.675
21	204.95	58.872	21	604.950	37.675
22	244.95	60.387	22	624.950	37.675
23	284.95	61.296	23	644.950	37.499
24	324.95	61.61	24	664.228	36.823
25	364.95	61.33			
26	404.95	60.453			
27	444.95	58.965			
28	484.95	56.831			
29	524.95	53.989			
30	544.95	52.274			
31	564.95	50.347			
32	584.95	48.191			
33	604.95	45.792			
34	624.95	43.127			
35	644.95	40.175			
36	664.228	36.823			

Table 1b: Two-element airfoil coordinates for Flap

	Upper surface			Lower surface	
S. No	X	Y	S. No	X	Y
1	525.044	5.861	1	525.318	3.949
2	525.239	8.877	2	526.028	2.155
3	527.335	14.519	3	528.701	-0.569
4	531.203	19.145	4	532.448	-1.177
5	541.406	25.583	5	546.63	1.399
6	552.788	29.677	6	562.056	4.105
7	564.577	32.425	7	579.216	6.943
8	576.538	34.301	8	600	10.032
9	594.618	35.993	9	619.852	12.542
10	612.761	36.729	10	638.703	14.42
11	630.922	36.762	11	656.473	15.658
12	649.076	36.244	12	673.092	16.313
13	664.188	35.462	13	688.516	16.397
14	680.329	33.281	14	702.619	16.115
15	696.342	30.283	15	715.409	15.449
16	710.473	27.407	16	736.798	13.474
17	728.501	23.462	17	752.322	11.227
18	743.015	19.938	18	761.737	9.478
19	764.894	13.547	19	764.888	8.869
20	764.888	8.869			

Table 2a: Pressure port locations on the main element

Upper surface _ Main element			Lower surface _ Mail element		
Pressure port No	X-Coordinate	Y-Coordinate	Pressure port No	X-Coordinate	Y-Coordinate
MU0	0	0	ML01	1.5	-6.6
MU01	1.16	5 6	ML02	8.3	-12
MU02	5.93	13.7	ML03	20	-14.5
MU03	11.3	19.23	ML04	31	-16.5
MU04	16.1	23.07	ML05	60.86	-20.8
MU05	27.6	30	ML06	90.5	-24
MU06	38	35.2	ML07	125	-26.5
MU07	47.5	38 9	ML08	150.4	-28.7
MU08	58.5	42.7	ML09	181.5	-30.15
MU09	69	45.7	ML10	211	-31.1
MU10	80	48.5	ML11	242.7	-31.6
MU11	91.3	50.4	ML12	273.3	-31.33
MU12	121.4	53.4	ML13	301.8	-30.5
MU13	151	55.6	ML14	331.83	-29
MU14	179	57.5	ML15	364.12	-26.5
MU15	211	59	ML16	394.2	-23.2
MU16	239	60	ML17	424.8	-19
MU17	267	61	ML18	454.8	-14.6
MU18	299	61.6	ML19	484	-9.3
MU19	328	61.6	ML20	514.6	-4.5
MU20	358	61.5	ML21	526.4	0.7
MU21	389	61	ML22	525	22.4
MU22	416	60.3	ML23	552	38
MU23	446	59	ML24	625	37.7
MU24	476.3	57.2			
MU25	507	55.45			
MU26	544	52.2			
MU27	563.2	50.7			
MU28	595.3	47			
MU29	618	44			
MU30	637	41.5			

Table 2b: Pressure port locations on the **flap**

Upper surface _ Flap			Lower surface _ Flap		
Pressure port No	X-Coordinate	Y-Coordinate	Pressure port No	X-Coordinate	Y-Coordinate
FU00	529.371	-1.199	FL01	539.145	-0.728
FU01	525.407	4.564	FL02	551.751	1.856
FU02	526.156	11.7	FL03	574.578	5.707
FU03	529.043	16.329	FL04	598.338	9.132
FU04	533.163	19.969	FL05	621.876	12.363
FU05	537.833	22.835	FL06	644.207	14.391
FU06	541.614	25.351	FL07	663.96	15.79
FU07	546.473	26.965	FL08	688.742	16.916
FU08	554.654	29.529	FL09	715.827	15.228
FU09	563.585	31.556	FL10	738.241	13.114
FU10	576.941	34.297	FL11	755.77	10.559
FU11	599.536	36.289			
FU12	621.459	36.121			
FU13	643.521	36.454			
FU14	666.051	35.113			
FU15	687.987	31.503			
FU16	712.202	26.733			
FU17	731.455	21.8			
FU18	747.178	18.495			

Table 3: $C_{l\,max}$ for different flap deflections at different overhangs.

	OH=0%C Gap=2.61%C	OH=+5.228%C Gap=2.61%C	OH=-1.3%C Gap=2.61%C
$\delta_f = 20^0$	Clmax=1.898 At $\alpha = 24^0$	Clmax=1.8105 At $\alpha = 24^0$	
$\delta_f = 25^0$	Clmax= 1.927 At $\alpha_x = 22^0$	Clmax=1.9197 At $\alpha = 24^0$	
$\delta_f = 30^0$	Clmax=2.0098 At $\alpha = 22^0$	Clmax=1.7886 At $\alpha = 22^0$	Clmax=1.7183 At $\alpha = 22^0$
Retracted configuration $C_{l\,max}$=1.2428 at $\alpha = 25^0$			

Appendix A

Scanners Calibration

The accuracy of the scanners is maintained through periodic on-line calibrations. A calibration before an experiment is done assure the highest accuracy of the system. A calibration process consists of pneumatically switching the scanner calibration manifold into calibrate mode and applying multiple known pressures to all the ports of each pressure scanner. Schematic diagram for calibration set-up for multiple pressure scanners is shown below. Piston pump pressurizes the pressure tank and controlled pressure is applied to the calibration ports of all the scanners.
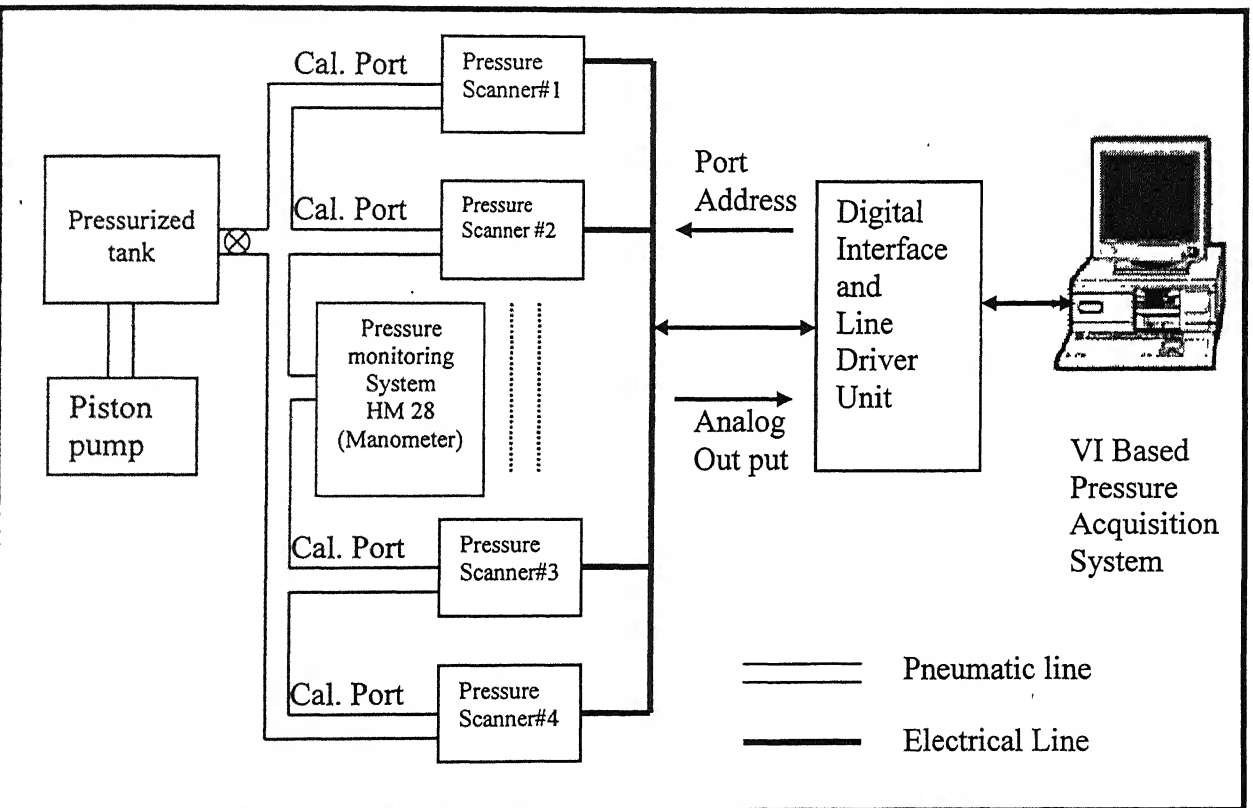
Schematic diagram of multiple pressure scanners calibration system

A set of applied pressures to the calibration ports of the scanners is measured using digital handheld monomer and is acquired using Scanners Calibration VI as shown below.The electrical analog outputs corresponding to applied pressures of each sensor with in the scanners are monitored on the front panel of calibration VI and the calibration data file is created for all the scanners and was saved in text file.

Scanner calibration.vi					

File Edit Operate Tools Browse Window Help

13pt Symbol

Input Parameters

Device ♦ 1

AI chan 0,1,2,3,4,5,6,7,8

Nsamples ♦ 250

NPort ♦ 32

Header string

Calibration of Scanners #1,2,3,4,5,6

START

Pressure Data

-0 00	0.02	-0 09	-0 03	0 00	-0 35
-0 01	0 01	-0 07	-0.04	-0.02	-0 33
0 01	-0 04	-0 02	-0 03	-0 01	-0 33
0 00	0.00	-0.08	-0 03	-0.02	-0 35
-0 02	0.00	-0 06	-0 04	-0.02	-0 37
-0 02	0 00	-0.11	-0.04	-0 02	-0 35
-0 00	-0.00	-0 09	-0.03	-0 02	-0 37
-0.01	0.01	-0.11	-0.01	-0.03	-0 34
-0 04	-0 01	0.03	-0.03	-0.03	-0 33
-0 04	-0 01	-0 06	-0 04	-0 02	-0 37
-0 02	-0 04	-0 07	-0.07	-0 02	-0 31
-0 04	-0 02	-0.07	-0.02	-0 00	-0 37
-0.02	-0.00	-0.08	-0.08	-0.02	-0.28
-0 02	-0.01	-0.09	-0.08	-0.03	-0.27

Front panel of Scanner's Calibration VI

Calculation of scanner Calibration coefficients

The calibration data for each of the scanner has been reduced to offset, sensitivity and non-linearity coefficients that are used to calculate unknown pressures. The following 2nd order Polynomial resulting from calibration is used to calculate the pressure during data acquisition.

$$P_x = C_0 + C_1 V_x + C_2 V_x^2$$

where P_x = pressure measured

C_0, C_1, C_2 = Calibration coefficients.

Front panel of the Scanner calibration Coefficients VI is shown below. Graph in the figure shows the linear curve fit for the scanner.
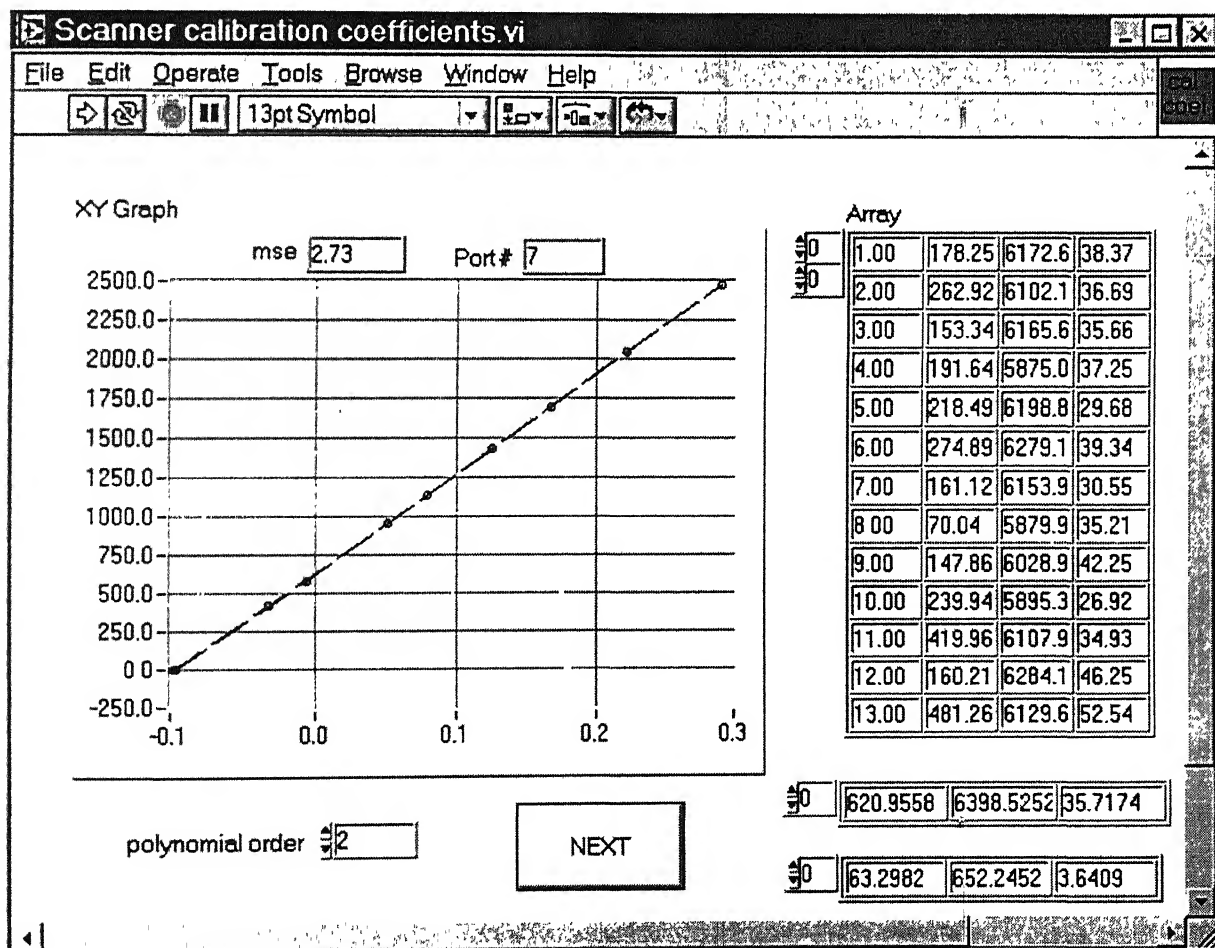
Front panel of Scanner's Calibration Coefficients VI

Calibration Coefficients for the six scanners are given below in the table.

| Scanner # 1 | | | | Scanner # 2 | | | |
Port #	C_0	C_1	C_2	Port #	C_0	C_1	C_2
1	151.954	6130.105	19.122	1	533.355	6229.118	11.715
2	248.583	6056.963	20.782	2	422.881	6040.405	23.570
3	140.351	6123.674	15.426	3	75.726	5950.431	15.459
4	151.434	5836.723	18.671	4	523.106	6168.336	26.434
5	212.507	6149.517	20.560	5	345.527	6271.519	17.653
6	234.998	6237.111	21.076	6	675.728	6226.155	11.551
7	173.849	6105.562	11.530	7	531.855	6349.273	12.485
8	48.558	5841.105	13.409	8	707.611	6374.995	11.220
9	145.046	5986.714	19.740	9	-243.035	6236.539	15.731
10	236.109	5848.519	18.378	10	335.387	6210.261	13.611
11	418.594	6059.435	18.663	11	416.565	6191.888	18.227
12	99.083	6246.688	20.402	12	413.129	6268.937	25.926
13	429.248	6091.678	20.366	13	464.725	6165.081	13.626
14	435.04	5879.156	17.945	14	561.665	6174.884	10.829
15	168.12	5839.900	10.966	15	332.846	6314.717	9.8230
16	121.916	5958.856	12.567	16	380.986	6052.855	9.1970
17	-181.447	6166.559	18.483	17	355.556	6350.002	13.852
18	75.106	6226.342	18.955	18	537.701	6181.971	7.920
19	36.979	6450.902	18.245	19	-17.838	6086.032	14.556
20	200.546	6286.821	23.378	20	754.223	6118.251	34.127
21	293.612	5904.128	19.266	21	426 681	6126.690	13.957
22	-290.311	6382.412	17.687	22	446.536	6162.882	13.011
23	67.152	6116.850	15.887	23	419.262	6050.545	12.809
24	637.943	6127.110	19.242	24	314.556	6215.223	24.704
25	-97.36	6355.871	14.175	25	536.999	6176.263	13.670
26	249.429	6168.432	19.182	26	334.347	6259.119	13.833
27	205.804	6100.635	22.078	27	323.341	5902.514	22.291
28	146.906	6029.321	19.394	28	-218.306	6042.115	19.379
29	212.955	6157.872	23.005	29	595.421	6136.155	10.552
30	243.128	5941.940	17.574	30	438.579	6191.080	14.006
31	-132.681	6075.966	10.075	31	603.835	6306.615	11.537
32	357.602	6074.738	15.601	32	704.902	6078.763	12.861

Scanner # 3				Scanner # 4			
Port #	C_0	C_1	C_2	Port #	C_0	C_1	C_2
1	54.617	5952.607	44.491	1	5.891	6118.911	34.862
2	179.507	6496.526	20.601	2	241.939	5725.350	34.241
3	124.686	6388.045	19.180	3	472.895	5755.370	33.797
4	167.313	6711.797	24.666	4	251.554	6145.292	39.556
5	194.911	6464.228	21.253	5	84.692	6067.719	34.954
6	199.292	6552.466	34.947	6	757.976	6127.885	39.823
7	167.681	6672.699	28.406	7	66.588	6025.660	35.397
8	222.026	6362.315	42.205	8	490.725	6045.194	35.294
9	261.374	6214.976	40.505	9	1.784	6124.583	34.171
10	182.4	6478.859	20.275	10	134.563	5933.164	33.624
11	205.197	6542.221	26.343	11	557.689	5838.005	37.076
12	50.516	6463.125	27.461	12	488.235	5824.721	31.310
13	179.164	6402.935	28.800	13	245.69	6281.614	38.822
14	236.144	6648.060	31.830	14	376.63	6252.814	44.150
15	182.528	6507.664	30.500	15	553.329	6266.696	38.172
16	82.504	6601.838	22.672	16	934.949	6118.382	41.990
17	-33.562	6565.391	41.511	17	228.739	5744.648	30.804
18	71.424	6503.574	52.345	18	169.822	5917.619	33.912
19	67.434	6302.700	27.643	19	183.634	5799.090	32.819
20	228.762	6663.809	22.882	20	500.989	5807.372	36.371
21	-106.929	7112.524	23.046	21	455.666	6188.247	49.960
22	48.261	6484.104	36.302	22	467.928	6092.550	40.989
23	190.751	6070.584	18.861	23	-260.372	6205.114	33.666
24	142.735	6290.883	16.5100	24	-64.869	6235.258	37.090
25	201.323	6291.503	21.054	25	273.408	5809.969	27.178
26	114.937	6451.677	51.685	26	107.855	6060.099	38.459
27	204.498	6554.422	25.578	27	215.943	5837.804	30.348
28	175.115	6605.154	26.578	28	408.129	5769.431	31.999
29	273.441	5975.881	29.289	29	278.237	5930.893	42.162
30	150.534	6027.637	34.261	30	529.34	6016.519	44.942
31	191.702	6295.671	18.006	31	181.292	6186.057	38.019
32	-274.716	6290.487	16.722	32	-217.267	6240.626	41.543

	Scanner # 5				Scanner # 6		
Port #	C_0	C_1	C_2	Port #	C_0	C_1	C_2
1	360.542	3039.255	13.388	1	-45.902	6745.023	83.554
2	292.854	2991.731	15.031	2	13.086	6695.405	67.486
3	382.442	2988.738	13.490	3	310.333	6725.051	53.758
4	339.923	3066.522	14.097	4	31.554	5964.884	19.068
5	311.016	3088.271	15.328	5	25.753	5915.894	35.240
6	305.179	2957.064	14.416	6	39.683	6322.131	86.117
7	372.114	3049.755	13.494	7	66.014	5988.852	31.020
8	156.661	2921.105	13.629	8	0.687	6282.441	84.546
9	268.684	3179.560	14.917	9	91.506	6542.576	60.905
10	405.11	2952.251	14.432	10	108.291	6673.641	77.706
11	300.969	3008.217	13.368	11	276.927	6520.960	51.256
12	403.656	3150.192	13.710	12	173.494	6116.147	53.891
13	219.328	3073.624	14.998	13	73.243	6093.826	49.449
14	474.302	3077.194	14.684	14	79.973	6159.651	40.830
15	280.106	3110.824	14.750	15	46.945	5894.917	40.280
16	383.682	3012.906	13.742	16	75.338	6228.997	62.528
17	248.367	3199.078	14.138	17	-194.349	6297.277	38.649
18	368.111	3027.936	14.826	18	-17.813	6114.938	61.775
19	279.869	2990.949	14.147	19	191.089	6231.842	39.836
20	351.592	2993.827	15.637	20	237.004	6288.726	66.964
21	344.412	3011.055	15.993	21	326.238	6341.591	54.508
22	386.222	3022.885	14.027	22	-63.406	6317.016	56.845
23	285.514	3134.627	14.272	23	131.511	6074.400	36.476
24	359.568	3066.388	13.919	24	280.407	6284.904	52.844
25	146.818	3064.204	13.044	25	13.194	6359.046	73.893
26	360.273	2969.452	14.391	26	43.54	5972.608	44.041
27	357.724	2974.592	13.183	27	28.212	6049.083	63.534
28	360.773	3052.981	13.104	28	265.151	6339.832	60.743
29	212.238	3009.943	14.668	29	-248.857	5920.924	29.231
30	221.308	3027.976	14.979	30	91.058	6301.585	47.901
31	318.996	2899.519	12.326	31	275.322	6083.289	47.817
32	294.636	3032.183	15.102	32	145.032	6346.625	49.867